A&A 672, A153 (2023)
https://doi.org/10.1051/0004-6361/202142217

Astronomy & Astrophysics

CO(2–1) survey at 9 pc resolution in the Small Magellanic Cloud*

H. P. Saldaño[1,2], M. Rubio[3], A. D. Bolatto[4,5,6], C. Verdugo[7], K. E. Jameson[8], and A. K. Leroy[9,10]

[1] Observatorio Astronómico de Córdoba, Universidad Nacional de Córdoba, 5000 Córdoba, Argentina
e-mail: hpablohugo@gmail.com
[2] Consejo Nacional de Investigaciones Científicas y Técnicas (CONICET), Godoy Cruz 2290, CABA, CPC 1425FQB, Argentina
[3] Departamento de Astronomía, Universidad de Chile, Casilla 36-D, Santiago, Chile
[4] Department of Astronomy and Joint Space-Science Institute, University of Maryland, College Park, MD 20742, USA
[5] Visiting Scholar at the Flatiron Institute, Center for Computational Astrophysics, NY 10010, USA
[6] Visiting Astronomer at the National Radio Astronomy Observatory, VA 22903, USA
[7] Joint ALMA Observatory (JAO), Alonso de Córdova 3107, Vitacura, Santiago de Chile
[8] Space and Astronomy, CSIRO, 26 Dick Perry Avenue, Kensington, WA 6151, Australia
[9] Department of Astronomy, The Ohio State University, 140 West 18th Avenue, Columbus, OH 43210, USA
[10] Center for Cosmology and Astroparticle Physics, 191 West Woodruff Avenue, Columbus, OH 43210, USA

Received 14 September 2021 / Accepted 2 January 2023

ABSTRACT

Context. The Small Magellanic Cloud (SMC) is the closest low-metallicity galaxy to the Milky Way where the dynamical state of molecular clouds can be analyzed.
Aims. Our aim is to present a CO(2−1) survey at ∼9 pc resolution obtained with the Atacama Pathfinder Experiment telescope in an extensive region (∼0.4 kpc^2) of the SMC and uniformly characterize the properties of the SMC clouds.
Methods. We used the CPROPS algorithm to identify the molecular clouds and estimate their main CO properties. We analyzed the characteristics of the SMC clouds by studying the scaling relations between the radii, velocity dispersions, luminosities, and virial masses. We also analyzed the mass spectrum of the SMC through the cumulative mass distribution. We used the dust-based total gas masses of SMC clouds presented in the literature to analyze the stability of the molecular clouds and also to estimate the CO-to-H_2 conversion factor for the SMC. We used young stellar objects (YSOs) and HII region catalogs in the literature and IR observations in public databases to inspect the star-forming regions in the SMC.
Results. We identified 177 molecular clouds within the SMC, of which 124 clouds are fully resolved with signal-to-noise ratios ≳5. We found that the CO luminosity of the identified clouds is $(1.3 \pm 0.2) \times 10^5$ K km s^{-1} pc^2 (representing at least 70% of the total CO luminosity of the region) and the corresponding gas mass from virial determination is $M_{\rm gas} = (1.5 \pm 0.5) \times 10^6\, M_\odot$. The scaling relationships show that the SMC clouds are (on average) less turbulent and less luminous than their inner Milky Way counterparts of similar size by a factor of approximately two and three, respectively, while for a fixed linewidth, the SMC clouds are overluminous by a factor of approximately 3.5. We found that the mass spectra of the SMC based on both the luminous mass and the virial mass are steeper than $\mathrm{d}N/\mathrm{d}M \propto M^{-2}$, suggesting that most of the molecular mass of the SMC is contained in low-mass clouds. Using the virial masses of the SMC CO clouds identified by CPROPS, we derived a CO-to-H_2 conversion factor of $\alpha_{\rm CO}^{\rm vir} = 10.5 \pm 5\, M_\odot\, (\mathrm{K\,km\,s^{-1}\,pc^2})^{-1}$, adopting the measured SMC CO(2−1)/CO(1−0) ratio of one. Regarding the dust clouds for which we had identified the corresponding CO emission, we determined an upper limit of the dust-based conversion factor for the SMC of $\alpha_{\rm CO}^{\rm dust} = 28 \pm 15\, M_\odot\, (\mathrm{K\,km\,s^{-1}\,pc^2})^{-1}$ at 12 pc resolution. These conversion factors, determined by two alternative methods, are about 2.5 and 6.5 times larger than the canonical Galactic conversion factor. For molecular clouds where there is both a dust and a virial mass, we found that the clouds appear to be in approximate gravitational virial equilibrium. Finally, we found that about half of the clouds identified by CPROPS are associated with ongoing star formation, either YSOs or HII regions, but also that close to half the clouds are not. Most of the YSOs in the clouds are in their first evolutive stages.

Key words. galaxies: dwarf – galaxies: individual: SMC – ISM: clouds – ISM: molecules

1. Introduction

The Small Magellanic Cloud (SMC), a nearby galaxy at ∼60 kpc (Hilditch et al. 2005), is an ideal laboratory for studying the link between high-mass star formation and the interstellar medium (ISM) in low-metallicity regions. The ISM of the SMC is characterized by a metallicity of ∼0.2 $Z_\odot$ (12+log(O/H) ≃ 8.0, Russell & Dopita 1992), a high gas-to-dust ratio (GDR) of ∼2000 (Roman-Duval et al. 2017) and a strong UV radiation field (up to ten times higher than that in the solar neighbourhood, Vangioni-Flam et al. 1980). It contains an extremely large amount of atomic gas and an extremely low fraction of molecular components (about 4% of the total mass of neutral gas (HI+He+metals) is molecular, see Jameson et al. 2016; Di Teodoro et al. 2019). All of these characteristics of the ISM make the SMC an environment analogous to the early Universe.

Measuring the amount of molecular hydrogen gas (H_2) in the SMC through observations of carbon monoxide (CO), the most common H_2 tracer, has been a real challenge in the last three

* Reduced datacubes and full Table 2 are available at the CDS via anonymous ftp to cdsarc.cds.unistra.fr (130.79.128.5) or via https://cdsarc.cds.unistra.fr/viz-bin/cat/J/A+A/672/A153

decades due to the ISM's characteristics. The first ^{12}CO(1−0) survey of the SMC was done by Rubio et al. (1991), mapping an area of 3×2 degrees at 8.8 arcmin resolution (154 pc) and finding large ^{12}CO (hereafter CO) complexes of sizes >100 pc from the southwest (SW) and the northeast (NE) of the bar of the galaxy. Later, with better spatial resolutions of ∼40″ (∼12 pc at the SMC distance) and 22″ (6.5 pc), an analysis of the CO(J = 1−0, 2−1) and ^{13}CO(J = 1−0, 2−1) toward pointed and small areas in the SMC was performed by Israel et al. (1993), Rubio et al. (1993b,a, 1996), and Muller et al. (2010). These authors found CO clouds with sizes between ∼10 and 40 pc and peak emission between ∼0.3 and 7 K. A CO(1−0) survey of the entire SMC was performed by Mizuno et al. (2001), mapping the emission in the SMC Bar and the SMC Wing (the transition to the Magellanic Bridge) with the NANTEN telescope at a coarser spatial resolution of 2.6′ (∼45 pc). At much better resolutions (∼1–2 pc), studies that used interferometric observations from the Atacama Large Millimeter Array (ALMA) telescope identified several tiny CO clouds in different regions of the SMC (e.g., Jameson et al. 2018; Fukui et al. 2020; Tokuda et al. 2021).

These observations in the SMC have unveiled very weak CO clouds with smaller beam-filling fractions than their Galactic counterparts and are consistent with other low-metallicity galaxies, such as WLM (Rubio et al. 2015) and NGC 6822 (Schruba et al. 2017). However, different resolutions and methodologies employed in studying the CO emission in the SMC have made it difficult to obtain a homogeneous set of physical cloud properties. In coarse resolution observations (Rubio et al. 1991, 1993a; Mizuno et al. 2001), the SMC giant molecular clouds (GMCs) exhibit CO luminosity several times smaller than those of the inner Milky Way with similar linewidth and virial mass, although they appear to be consistent with the Galactic size-linewidth relation. Later studies at higher resolution and sensitivity (Bolatto et al. 2008) using the CPROPS decomposition (Rosolowsky & Leroy 2006), however, show that the SMC clouds are under the Galactic size-linewidth relation and have CO luminosities similar to their virial mass. This suggests that measurements that reach the spatial scale of the CO-dominated portion of GMCs yield conversion factors that are close to Galactic values, even in lower metallicity environments such as the SMC.

Environmental conditions also play a role in shaping the properties of clouds. The high pressure in galaxy centers may drive the equilibrium in the direction of larger velocity dispersions for a given size (Oka et al. 2001; Colombo et al. 2014; Utomo et al. 2015; Leroy et al. 2015). A similar result has been found near the R136 stellar cluster in 30 Doradus in the Large Magellanic Cloud (LMC) by Kalari et al. (2018). Alternatively, environments of low pressure, such as the outer Milky Way disk with small and transient clouds, display linewidths too large for their masses (Heyer et al. 2001). Evidence of the dependence of molecular parameters on the environment inside the SMC was investigated by Muller et al. (2010), finding that CO clouds are fainter and have narrower linewidths in the NE region than in the SW region. We note, however, that the dynamical properties of the molecular ISM depend on spatial resolution (e.g., Leroy et al. 2016). For this reason, homogeneous studies that have a common spatial resolution and uniform algorithms are important to obtaining consistent results across a galaxy.

Our goal is to characterize the CO clouds of the SMC at 9 pc resolution and examine their properties and dynamical states using CO(2−1) observations obtained with the Atacama Pathfinder Experiment (APEX) telescope. In Fig. 1, we show the observed regions in the SMC superimposed on the *Herschel* Space Observatory 160 μm cold dust image (Gordon et al. 2014). These regions are located toward the brightest dust emission sources and the highest H_2 column density of the galaxy (see Figs. 2 and 3). The two largest observed regions are in the SW and NE of the SMC-Bar, frequently referred to as the SW-Bar and NE-Bar, respectively. We also mapped several smaller regions, N66 in the NE and DarkPK in the SW, as well as three regions located in the Wing of the SMC, N83, NGC 602, and N88. These maps cover regions with a large range of activity properties: The NE region is active but likely older and shows weaker clouds (Muller et al. 2010). N66 is the brightest HII region of the SMC with ongoing strong high-mass star formation (Simon et al. 2007; Rubio et al. 2018). DarkPK is a quiescent region with a lot of molecular gas but very low activity dominated by "CO-dark" molecular gas (Jameson et al. 2018), while N83, NGC 602, and N88 are isolated high-mass star-forming regions in the SMC Wing (Bolatto et al. 2003; Carlson et al. 2011; Ward et al. 2017). The high sensitivity and area (∼0.4 kpc^2) coverage of these observations permit us to obtain a large uniform sample of CO clouds within the SMC.

We aim to analyze the physical condition of GMCs using these homogeneous data and a consistent methodology. We analyzed the size-linewidth relation of the sample, the luminosity scaling relations ($L_{CO} - \sigma$ and $L_{CO} - R$), and the virial mass luminosity relation ($M_{vir} - L_{CO}$) that have been well-defined for Galactic and extra-galactic GMCs (Solomon et al. 1987; Bolatto et al. 2008; Colombo et al. 2014; Leroy et al. 2015). These scaling relations provide further constraints for cloud formation models (e.g., Camacho et al. 2016).

The Milky Way size-linewidth relationship is frequently used to study the dynamic and equilibrium turbulence conditions of molecular clouds. For inner Milky Way GMCs, Solomon et al. (1987) found the following relation:

$$\sigma_v = 0.72\, R^{0.5}\ \mathrm{km\,s^{-1}}, \tag{1}$$

which indicates similar surface densities of clouds in gravitational virial equilibrium. This Galactic relation is also interpreted as evidence of equilibrium supersonic turbulence conditions in a highly compressible medium (Bolatto et al. 2013). Observations also suggest that molecular clouds in different galaxies generally follow power-law relationships, similar to those defined by Solomon et al. (1987) as:

$$L_{CO} = 25\, R^{2.5}\ \mathrm{K\,km\,s^{-1}\,pc^2}, \tag{2}$$

$$L_{CO} = 130\, \sigma_v^5\ \mathrm{K\,km\,s^{-1}\,pc^2}, \tag{3}$$

and

$$M_{vir} = 39\, L_{CO}^{0.8}\, M_\odot, \tag{4}$$

for the inner Milky Way clouds. In Eqs. (2) and (3), R and σ are expressed in pc and km s^{-1}, respectively, while Eq. (4), (the Galactic mass–luminosity relation) employs L_{CO} in units of K km s^{-1} pc^2.

In Sect. 2, we describe the APEX observations and data reduction, as well as the complementary data used in the paper. In Sect. 3, we summarize the methodology used to identify the molecular clouds and the main equations used to determine the

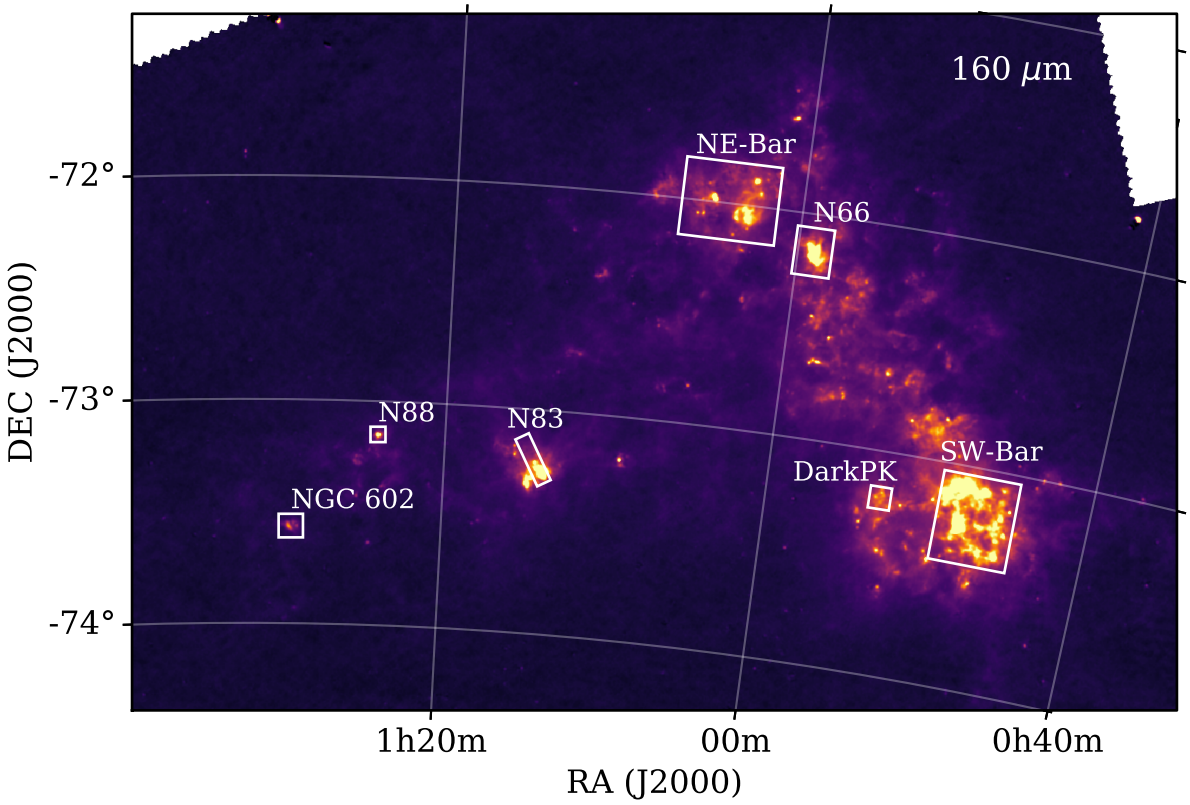

Fig. 1. Surveying CO emission in the SMC. The white boxes outline the seven regions where the CO(2−1) emissions were mapped with the APEX telescope. The background image of SMC is at 160 μm from HERITAGE *Herschel* Space Observatory Key Project (Gordon et al. 2014).

molecular parameters. In Sect. 4, we show the main results from the analysis of the scaling relations of the SMC clouds. We examine the CO association with young stellar objects (YSOs) and HII regions. We also present the analysis of the mass spectrum of the SMC through the cumulative mass distribution. In Sect. 5, we discuss the dynamical states of the SMC clouds, the CO-to-H_2 conversion factors of the galaxy, the observed features in the scaling relation of the SMC, and the comparison of the SMC cloud with those of other low-metallicity galaxies. Finally, in Sect. 6, we present a summary and conclusions.

2. Observations

2.1. APEX data

Seven regions of SMC, two in the northeast region (NE-Bar and N66), other two in the southwest region (SW-Bar and DarkPK), and three in the Wing (N83, NGC 602, and N88) were observed with APEX, a 12 m diameter millimeter-wave telescope located in Llano de Chajnantor, Chile (Güsten et al. 2006).

The observations were done in the ^{12}CO(2−1) molecular lines (230.538 GHz) using the Swedish Heterodyne Facility Instrument, APEX-1, under good weather conditions in June 2014 for the SW region (C93.F-9711-2014), and during 2015 for the NE and Wing regions (C.095F-9705A-2015). The half power beam width (HPBW) of the APEX-1 instrument is ∼27.5″ at ^{12}CO(2−1) frequency (Vassilev et al. 2008). Typical system temperatures were between 120 and 200 K. All the observations were conducted using the total power on-the-fly mode with a dump and grid spacing of 9″ and using a reference point free of CO(2−1), for background subtraction of each field, with a velocity resolution of 0.1 km s^{-1} and sensitivity of 50–150 mK rms, depending on the observed region.

The data reduction was performed according to the standard procedure of the CLASS software, Gildas.[1] The antenna temperature, T_A, was transformed to brightness temperature of the main beam ($T_{mb} = T_A/\eta_{mb}$) using a main beam efficiency $\eta_{mb} = 0.7$ for APEX-1. In the final reduction, the data were obtained with a spatial resolution of HPBW = 30″ (∼9 pc) and smoothed to a common velocity resolution of $\Delta V = 0.25$ km s^{-1} to improve the S/N. A mainly linear polynomial was employed for baseline fitting except in some cases where a third-order polynomial was used. The rms of all regions are between ∼0.1 and 0.7 K. Table 1 summarizes the corresponding observational parameters, including the equatorial coordinates and the field-of-view (FoV in Col. 5) for each region.

The observation in the SW-Bar region was combined with additional APEX observations of three 180″ × 600″ smaller maps in the same area, namely, N22 (RA=00:47:53.7, Dec= −73:17:54.8, PA=20°); SWBarS (RA=00:45:23.4, Dec= −73:21:43.3, PA=10°); and SWBarN (RA=00:48:17.4, Dec= −73:05:26.3, PA=145°). All observations were performed in the same program C.93F-9711-2014. These maps, observed with the same velocity resolution $\Delta V = 0.1$ km s^{-1} as the SW-Bar big map but with a higher sensitivity (rms = 0.05 K), were similarly reduced and smoothed to a velocity resolution of ΔV = 0.25 km s^{-1}. The combination of these three maps with the SW-Bar full map improved the S/N to about half of the rms obtained from the SW map in the overlapping areas.

[1] http://www.iram.fr/IRAMFR/GILDAS/

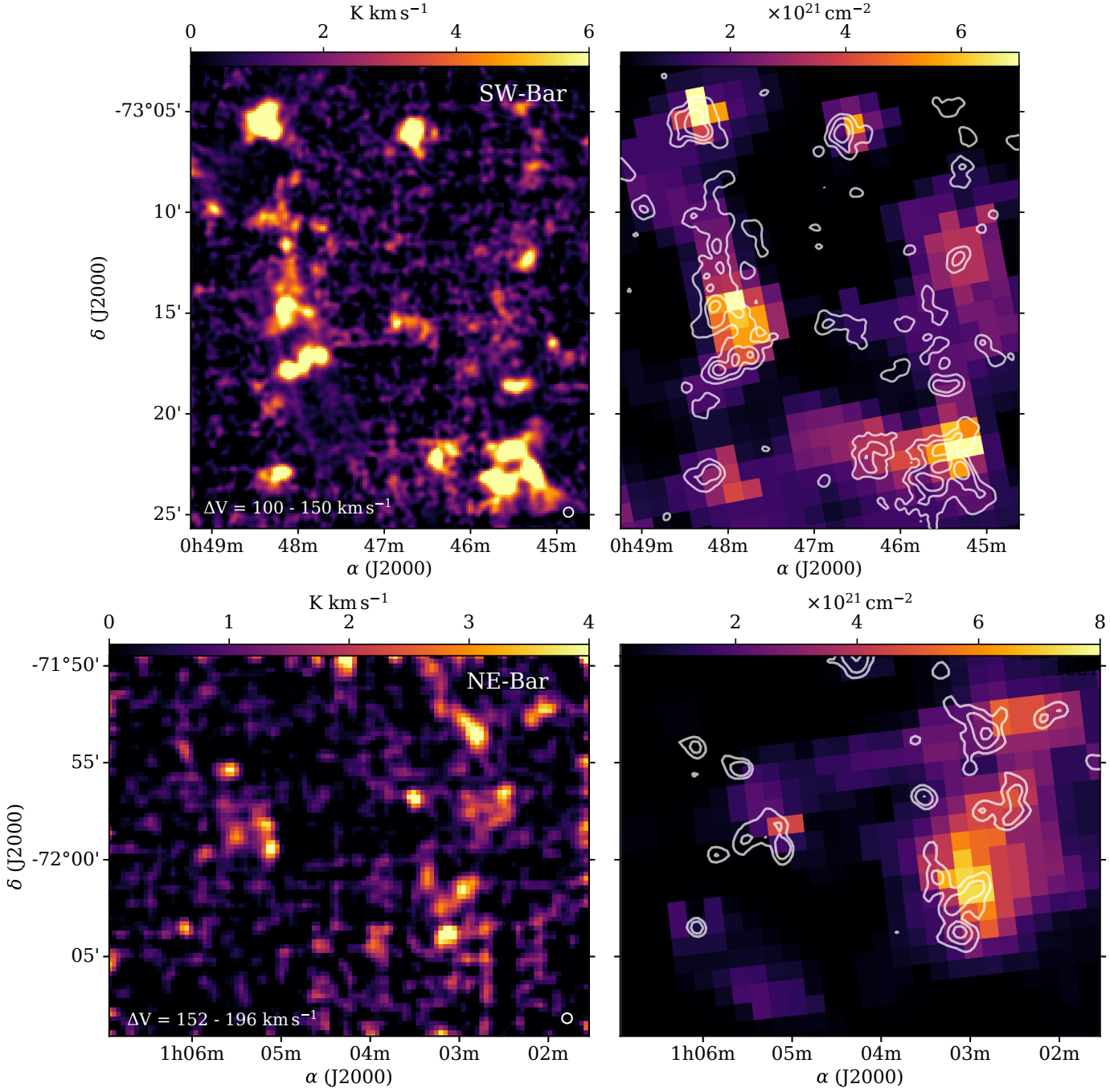

Fig. 2. Integrated CO(2−1) emission toward SW-Bar (top) and NE-Bar (bottom) regions. Only for this figure, both CO maps were smoothed with a Gaussian kernel of a radius of 2 pixels to improve the S/N. The beam size (30″ or ∼9 pc at the SMC distance) and the integration range (ΔV) are indicated at the bottom of the left panels. In the right panels, the integrated CO contours (determined with the moment masked method, see Sect. 4) are overlapped to the dust-based total column density (N_{H_2}) from Jameson et al. (2016). The CO contours in the SW and NE regions correspond to emissions at 1.5, 4.5, and 10.0 K km s^{-1} and 1.0, 2.0, and 4.5 K km s^{-1}, respectively.

2.2. Complementary data

We compared our CO observations with indicators of recent star formation in the SMC. For this comparison we used the Infrared Array Camera 8 µm map from the *Spitzer* project Surveying the Agents of Galaxy Evolution (Gordon et al. 2011). The 8 µm emission is dominated by polycyclic aromatic hydrocarbons (PAH) bands excited by high UV radiation fields coming from massive stars creating photo-dissociated regions (PDRs). We also used an Hα image from the Magellanic Cloud Emission-Line Survey (MCELS; Winkler et al. 2015) to compare the CO emission with ionized interstellar structures. The far-infrared and the millimeter emissions were also used as important indicators of star formation due to their large fractions of dust-absorbed starlight. We used the far-infrared map at 160 µm from the HERITAGE *Herschel* Key Project (Gordon et al. 2014) and the AzTEC 1.1 mm dust continuum survey of the SMC carried out by Takekoshi et al. (2017) at a Gaussian beam of 40″ (∼12 pc).

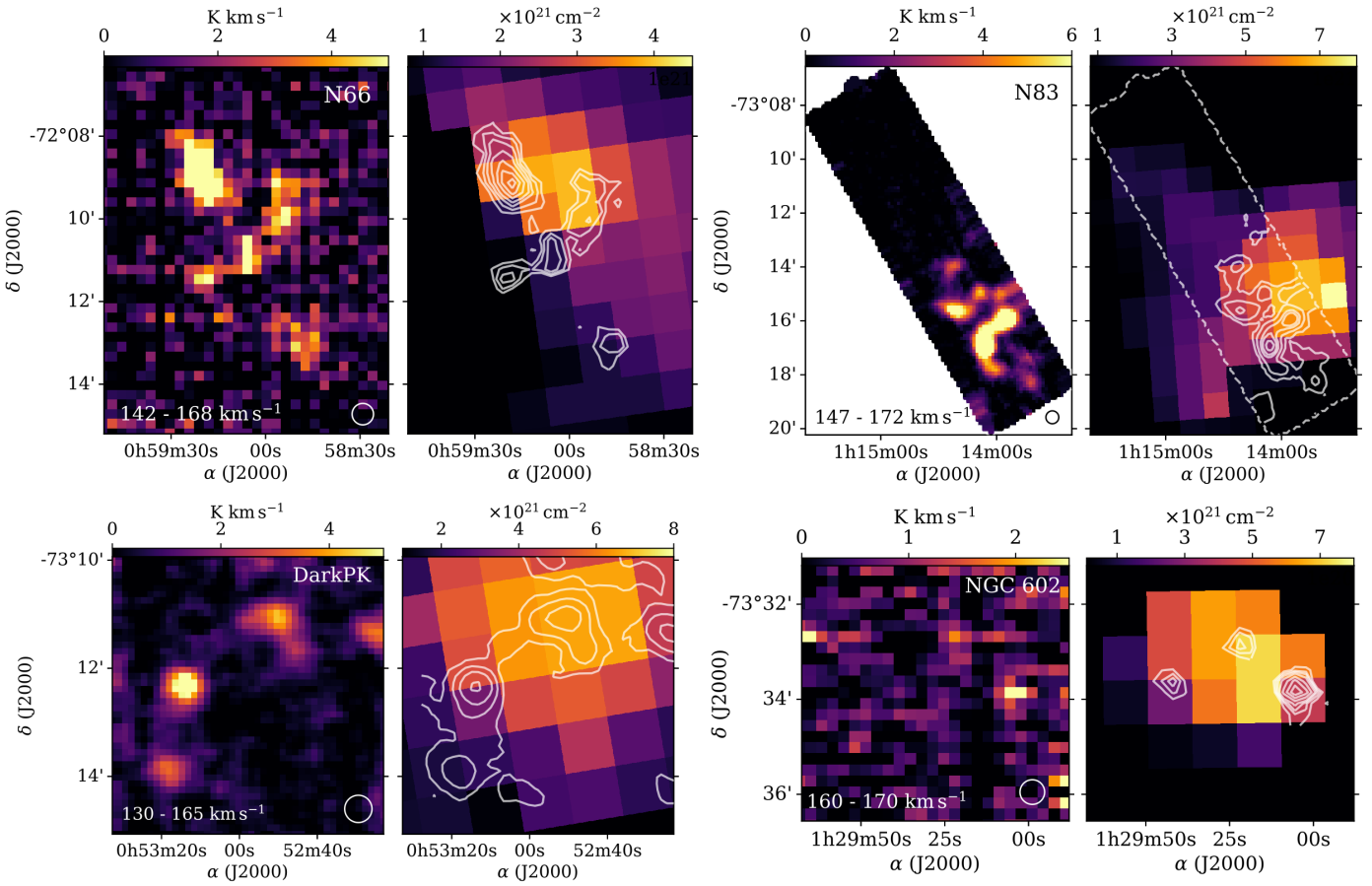

Fig. 3. Integrated CO(2−1) emission toward N66, N83, DarkPK, and NGC 602. The beam width of 30″ (~9 pc at the SMC distance) and the integrated velocity range are shown at the bottom of the left panels of each region. The CO contours in the right panel of N66 are at 1.6, 2.6, 4.0, 5.7, 8.6, 11.4, and 14.3 K km s^{-1}. In N83, the contours are at 1, 3, 7, 10, and 15 K km s^{-1}. In DarkPK, the CO contours take values of 0.5, 1.5, 3.0, and 6.0 K km s^{-1}. In NGC 602, the contours take values of 0.4, 0.5, 0.6, 0.9, 1.3, 1.7, and 2.1 K km s^{-1}. All of these contours were determined with the moment mask method (see Sect. 4).

Table 1. Observational characteristics of SMC regions.

SMC	Regions	RA (hh:mm:ss.s)	Dec (dd:mm:ss.s)	FoV (′×′)	PA (deg)	$V_{\rm lsr}$ (km s^{-1})	$T_{\rm rms}$ [(a)] (K)
SW	SW-Bar	00:46:55.8	−73:14:11.9	20.9 × 24.6	00	120.0	0.22
	DarkPK	00:52:56.5	−73:12:30.6	5.5 × 5.8	00	150.0	0.10
NE	NE-Bar	01:04:13.6	−71:59:25.2	24.8 × 19.7	00	167.0	0.24
	N66	00:59:05.9	−72:10:04.6	9.0 × 11.9	00	160.0	0.30
Wing	N83	01:14:29.5	−73:13:26.5	4.1 × 13.8	+30	161.7	0.10
	NGC 602	01:29:27.1	−73:33:51.2	5.8 × 5.8	00	166.5	0.30
	N88	01:24:08.5	−73:08:56.6	3.0 × 3.0	00	148.0	0.70

Notes. [(a)]The main brightness temperature $T_{\rm rms}$ is calculated in 0.25 km s^{-1} spectral resolution.

3. Methodology

In all regions, we applied the CPROPS algorithm developed by Rosolowsky & Leroy (2006) to identify and decompose the CO distribution into molecular clouds. In Appendix A, the identification and decomposition procedure applied to our data cubes are explained in more detail. Once the clouds were identified, CPROPS determined their main properties, such as central velocities, sizes, velocity dispersion, and fluxes through the moment method. This method uses the distribution of the emission in a cloud within a position-position-velocity data cube and does not assume a previous functional shape of the cloud. The CPROPS algorithm corrects the quoted properties for sensitivity and convolution biases.

To determine the size of the clouds, we used the Solomon et al. (1987) definition: $R \simeq 1.91\,\sigma_{\rm r}$. Here, $\sigma_{\rm r} = \sqrt{\sigma_{\rm maj}\,\sigma_{\rm min}}$, where $\sigma_{\rm maj}$ and $\sigma_{\rm min}$ are the rms sizes of the intensity distribution along the two spatial dimensions (Eq. (9) from Rosolowsky & Leroy 2006). For the clouds that are more elongated in one axis than the telescope beam (extrapolated $\sigma_{\rm min} < \sigma_{\rm beam}$) and

consequently not well resolved, CPROPS could not estimate their sizes. In such cases, we assumed the extrapolated $\sigma_{\rm min} = \sigma_{\rm beam}$ to be an upper limit in this axis, and the new rms size was given by $\sigma_{\rm r} = \sqrt{\sigma_{\rm maj}\,\sigma_{\rm beam}}$, and was then deconvolved in the standard way:

$$\sigma_{\rm r,upp} = \sqrt{\sigma_{\rm r}^2 - \sigma_{\rm beam}^2}. \quad (5)$$

This upper limit rms size was also multiplied by 1.91 to estimate the upper limit radius ($R_{\rm upp}$) of clouds. The velocity dispersion (σ_v) of each cloud, was calculated through Eq. (10) from Rosolowsky & Leroy (2006) in km s^{-1} units.

The luminosity of the molecular gas was given by:

$$L_{\rm CO(1-0)}[{\rm K\,km\,s^{-1}\,pc^2}] = F_{\rm CO(1-0)}(0\,{\rm K})[{\rm K\,km\,s^{-1}\,arcsec^2}](d[{\rm pc}])^2 \times \left(\frac{\pi}{180\times 3600}\right)^2, \quad (6)$$

where $F_{\rm CO(1-0)}(0\,{\rm K})$ is the flux of the cloud extrapolated to $T_{\rm rms} = 0$ K and d is the distance of the galaxy in parsec. In the following, we consider that the CO(2−1)/CO(1−0) integrated line brightness ratio is, on average, equal to 1.0 in the Magellanic Clouds (Rubio et al. 2000; Israel et al. 2003; Bolatto et al. 2003; Herrera et al. 2013; Tokuda et al. 2021), with variation between ∼10 and 30%. Thus, with this measured ratio, $L_{\rm CO(2-1)} \simeq L_{\rm CO(1-0)}$.

Another important parameter is the virial mass of the clouds. Assuming that clouds can be approximated by a self-gravitating sphere with a density profile $\rho \propto r^{-1}$ and discarding external force supports, such as magnetic fields and/or external pressure, the virial mass was given by the formula (Solomon et al. 1987):

$$M_{\rm vir} = 1040\,\sigma_v^2\,R\,(M_\odot), \quad (7)$$

where σ_v and R are the corrected velocity dispersion in km s^{-1} and radius in parsec, respectively. We also calculated the luminous mass of the clouds by using the $L_{\rm CO}$ and the Galactic CO-to-H_2 conversion factor $\alpha_{\rm CO} = 4.36\,M_\odot\,({\rm K\,km\,s^{-1}\,pc^2})^{-1}$ (which includes the He mass contribution; Bolatto et al. 2013) as follows:

$$M_{\rm lum} = L_{\rm CO}\,\alpha_{\rm CO}. \quad (8)$$

To determine the uncertainties of the parameters, the bootstrapping technique was used through CPROPS adding the BOOTSTRAP keywords. For clouds that were not well resolved, we used the error propagation to estimate the error in the upper limit radius and virial mass.

4. CO analysis and results

The left panels of Figs. 2 and 3 show the CO emission in the observed regions of the SMC. These CO maps were obtained by integrating the CO cubes within velocity ranges that included all molecular clouds detected in each region (see Mizuno et al. 2001). For SW-Bar and NE-Bar, the velocity ranges are 100–150 km s^{-1} and 152–196 km s^{-1}, respectively. While for N66 and N83, the velocity ranges are 142–168 km s^{-1} and 147–172 km s^{-1}, and finally, DarkPk and NGC 602 were integrated between 130–165 km s^{-1} and 160–170 km s^{-1}, respectively. All velocities are in $V_{\rm lsr}$. Our observations also include the N88 region with a single CO cloud detected between 145 and 150 km s^{-1}. N88 is shown in Appendix B.1.

To better display the CO emission in Figs. 2 and 3, we used the moment masking method optimized for CO spectral line surveys (for a detailed description of the method, see Dame 2011). With this method, small CO clouds with narrow velocity linewidth (few spectral channels) are recovered by integration over large velocity ranges. The moment-masked CO emissions are shown as contours in Figs. 2 and 3, superimposed on the dust-based H_2 column density ($N_{\rm H_2}$) map at ∼10 parsec resolution from Jameson et al. (2016), except for N88 where no H_2 column density map has been derived. In general, both figures show CO emission toward high H_2 column densities. Interestingly, additional small, isolated molecular clouds were detected for the first time in this work that are not present in the $N_{\rm H_2}$ map.

4.1. Molecular cloud parameters

In this section, we analyze the properties of the molecular clouds identified by CPROPS (Rosolowsky & Leroy 2006). The physical parameters of the CO clouds are listed in Table 2 where the Right Ascension and Declination in J(2000), the radius (R), the local-standard of rest velocity ($V_{\rm lsr}$), the velocity dispersion (σ_v), the peak temperature ($T_{\rm peak}$), the integrated CO(2−1) intensity ($I_{\rm CO}$), the CO(2−1) luminosity ($L_{\rm CO}$), and the virial mass ($M_{\rm vir}$) are included. These parameters were obtained using CPROPS and were corrected for sensitivity and resolution bias. To avoid redundancy in the analysis of these parameters, and for simplicity, we refer the clouds that belong to the SW-Bar and DarkPK as SW clouds; the clouds of the NE-Bar and N66 as NE clouds; and the clouds belonging to N83, NGC 602, and N88 as Wing (WG) clouds. In our analysis, we identified 177 CO clouds in the SMC, with 102 SW clouds, 47 NE clouds, and 28 WG clouds. The total luminosity of the 177 CO clouds is $(1.3 \pm 0.2)\times 10^5$ K km s^{-1} pc^2. To estimate the total CO emission, irrespective of whether it is in CPROPS identified clouds, we produced an integrated intensity map that included all beams with a $S/N > 3$. The resulting total luminosity in the region is 1.9×10^5 K km s^{-1} pc^2, likely an upper limit since the presence of noise tends to bias the estimate toward higher values (although probably not substantially). Comparing these two numbers, we estimated, that at most, ∼30% of the CO emission is not assigned to CO clouds by CPROPS.

Out of the total sample, 124 clouds (70%) are well resolved with nondeconvolved radii of $R \gtrsim 5.0$ pc and S/N higher than 5.0. A radius of 5.0 pc corresponds to a deconvolved radius of $R \simeq 2.2$ pc and was considered as our size resolution limit. The relative error in R of these well-resolved clouds are typically between 10 and 30%, with only a few clouds exceeding these values. Clouds with smaller radii than 2.2 pc have high uncertainties (≳100%) that strongly affect their virial mass determination. Therefore, the R and $M_{\rm vir}$ for these clouds are considered as undefined values in Table 2. Another 28 clouds have S/Ns between three and five, and thus the accuracy of the parameter determination deteriorates, producing large underestimations in their radius and linewidth. In the following analysis, we used only the 124 well-resolved clouds (deconvolved $R \gtrsim 2.2$ pc and $S/N > 5$).

Figure 4 shows the histograms of the velocity dispersion, radius, CO luminosity, and virial mass for the well-resolved high S/N clouds. The median values of each parameter for the total sample are the following: $\sigma_v = 1.05 \pm 0.23$ km s^{-1}, $R = 5.8 \pm 2.0$ pc, $L_{\rm CO} = (5.8 \pm 3.7)\times 10^2$ K km s^{-1} pc^2, and $M_{\rm vir} = (6.6 \pm 5.0)\times 10^3\,M_\odot$ (see Table 3). The distributions of

Table 2. Physical parameters of molecular clouds in SMC.

ID	RA (hh:mm:ss.s)	Dec (dd:mm:ss)	$R^{(a)}$ (pc)	$V_{\rm lsr}$ (km s^{-1})	σ_v (km s^{-1})	$T_{\rm peak}$ (K)	$I_{\rm CO(2-1)}$ (K km s^{-1})	$L_{\rm CO(2-1)}{}^{(b)}$ (caption)	$M_{\rm vir}{}^{(a)}$ ($10^3\,M_\odot$)
1	00:44:57.6	–73:10:07	2.9 ± 1.1	132.3 ± 1.1	1.0 ± 0.3	1.5 ± 0.2	66.7 ± 14.7	2.8 ± 0.6	3.0 ± 2.0
2	00:45:00.4	–73:16:45	12.5 ± 1.3	108.6 ± 1.4	1.2 ± 0.1	2.0 ± 0.2	289.3 ± 20.4	12.2 ± 0.9	18.7 ± 4.3
3	00:45:02.5	–73:24:06	10.8 ± 0.9	126.4 ± 1.4	1.2 ± 0.1	1.8 ± 0.2	252.5 ± 17.9	10.7 ± 0.8	16.2 ± 3.4
4	00:45:08.7	–73:20:37	...	125.8 ± 1.2	1.1 ± 0.3	0.9 ± 0.2	45.5 ± 12.6	1.9 ± 0.5	...
5	00:45:10.5	–73:24:39	6.8 ± 1.3	128.1 ± 1.2	1.0 ± 0.1	1.5 ± 0.2	118.6 ± 10.7	5.0 ± 0.5	7.1 ± 2.4
6	00:45:11.8	–73:21:21	4.3 ± 0.9	122.8 ± 1.0	0.8 ± 0.3	1.1 ± 0.2	74.2 ± 30.8	3.1 ± 1.3	2.9 ± 2.7
7	00:45:14.9	–73:06:13	6.4 ± 0.8	102.7 ± 1.2	1.0 ± 0.2	1.7 ± 0.3	119.6 ± 24.1	5.1 ± 1.0	6.7 ± 3.2
8	00:45:16.1	–73:20:27	2.5 ± 1.2	120.9 ± 1.7	1.5 ± 0.4	0.9 ± 0.2	45.1 ± 14.1	1.9 ± 0.6	6.1 ± 3.9
9	00:45:16.4	–73:23:07	13.0 ± 0.6	126.9 ± 2.9	2.5 ± 0.1	3.8 ± 0.2	1358.6 ± 47.7	57.5 ± 2.0	84.5 ± 7.6
10	00:45:18.1	–73:08:35	2.6 ± 1.2	110.7 ± 1.0	0.9 ± 0.2	1.5 ± 0.3	52.6 ± 14.3	2.2 ± 0.6	2.2 ± 1.5
11	00:45:18.3	–73:07:44	...	108.2 ± 0.8	0.7 ± 0.5	1.1 ± 0.3	32.2 ± 16.9	1.4 ± 0.7	...
12	00:45:18.6	–73:07:45	5.4 ± 1.8	103.5 ± 1.9	1.6 ± 0.3	1.8 ± 0.3	134.2 ± 19.0	5.7 ± 0.8	14.4 ± 7.7
13	00:45:20.4	–73:21:06	3.3 ± 1.0	116.0 ± 1.3	1.1 ± 0.1	2.1 ± 0.2	154.8 ± 10.5	6.5 ± 0.4	4.2 ± 1.7
14	00:45:21.2	–73:12:20	6.2 ± 0.8	123.1 ± 1.3	1.1 ± 0.1	3.5 ± 0.3	339.7 ± 19.8	14.4 ± 0.8	7.8 ± 2.0
15	00:45:21.3	–73:18:27	...	116.3 ± 1.4	1.2 ± 0.2	1.5 ± 0.2	85.9 ± 9.1	3.6 ± 0.4	...
...	...	...	...	...	...	...	...	...	...
...	...	...	...	...	...	...	...	...	...
176	01:29:20.7	–73:32:52	3.8 ± 3.2	162.0 ± 0.4	0.4 ± 0.2	0.9 ± 0.2	9.8 ± 2.6	1.7 ± 0.4	0.5 ± 0.8
177	01:29:42.4	–73:33:46	2.8 ± 1.3	166.8 ± 0.5	0.5 ± 0.2	1.1 ± 0.2	5.3 ± 1.4	0.9 ± 0.2	0.7 ± 0.7

Notes. $^{(a)}$Undefined values in the R and $M_{\rm vir}$ columns correspond to unresolved clouds (i.e., clouds with radii lower than the resolution limit). $^{(b)}L_{\rm CO}$ is in unit of 10^2 K km s^{-1} pc^2. The full table is available at the CDS.

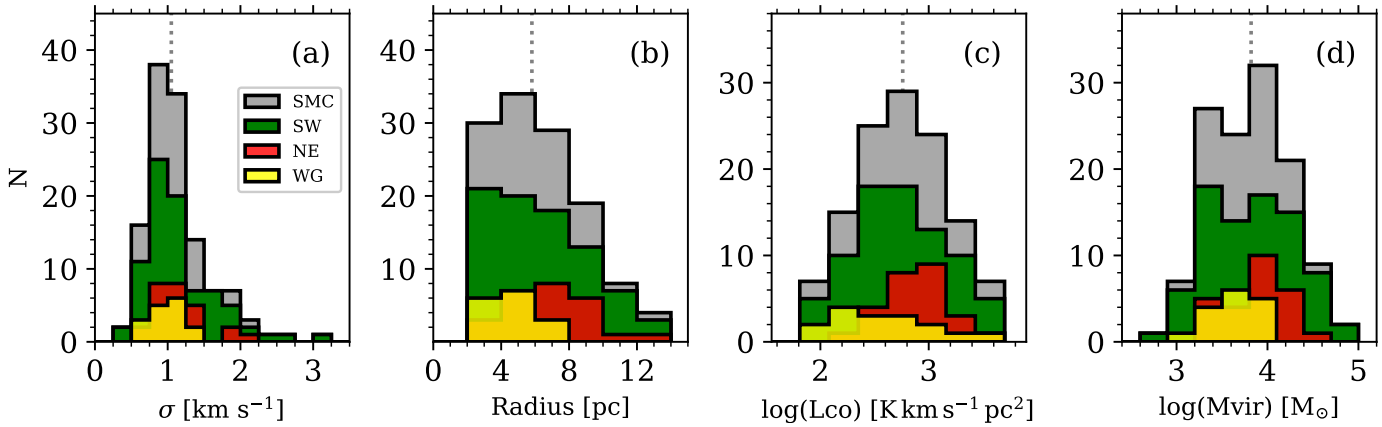

Fig. 4. Histogram of velocity dispersion σ_v (a), radius (b), CO luminosity (c), and virial mass (d) for SMC clouds (gray histograms) and for clouds in the SW (green), NE (red), and WG (yellow) regions. These histograms belong to the well-resolved clouds with $R \gtrsim 2.2$ pc and $S/N \gtrsim 5$. The vertical dotted line in each panel indicates the median of the parameter given in Table 3 for the total sample. These parameters were corrected for sensitivity and resolution biases from observations at 9 pc resolution.

the cloud parameters for the three regions, SW, NE, and WG, are also shown. Although these histograms differ in sample size, the parameter distributions are centered in almost similar median values. Despite the lower number of clouds in the NE and WG regions, with respect to the number of SW clouds, we quantified the comparison between the SW, NE, and WG samples by applying the Kolmogorov–Smirnov (K–S)[2] statistical test. We found that the chance that the R and $M_{\rm vir}$ histograms of the WG clouds is the same as the ones of the NE and SW histograms is very low (p-value ~ 0.03). In effect, Fig. 4 shows that there is a preponderance of the WG clouds to be smaller and less massive than the clouds in the other regions. Of course, a large number of clouds is required to confirm this result.

4.2. Scaling relations of the SMC clouds

In the following, we analyze the scaling relations (in log-log scale) between the velocity dispersion, radius, luminosity, and virial mass of the SMC clouds. We determined the best fit of each relationship by using a nonparametric (bootstrapping) method. With this method, we fit a linear function to N different X–Y data set of dimension k that was chosen randomly from the original data set with a similar dimension. The method provides N slightly different models, which are used to create a confidence interval for the slope and intersect. From the distribution of the fitted parameters, we estimated the mean of the slope and the

[2] The K–S test is based on the "null hypothesis" that indicates that two sets of values are from the same distribution if p-value > 10%.

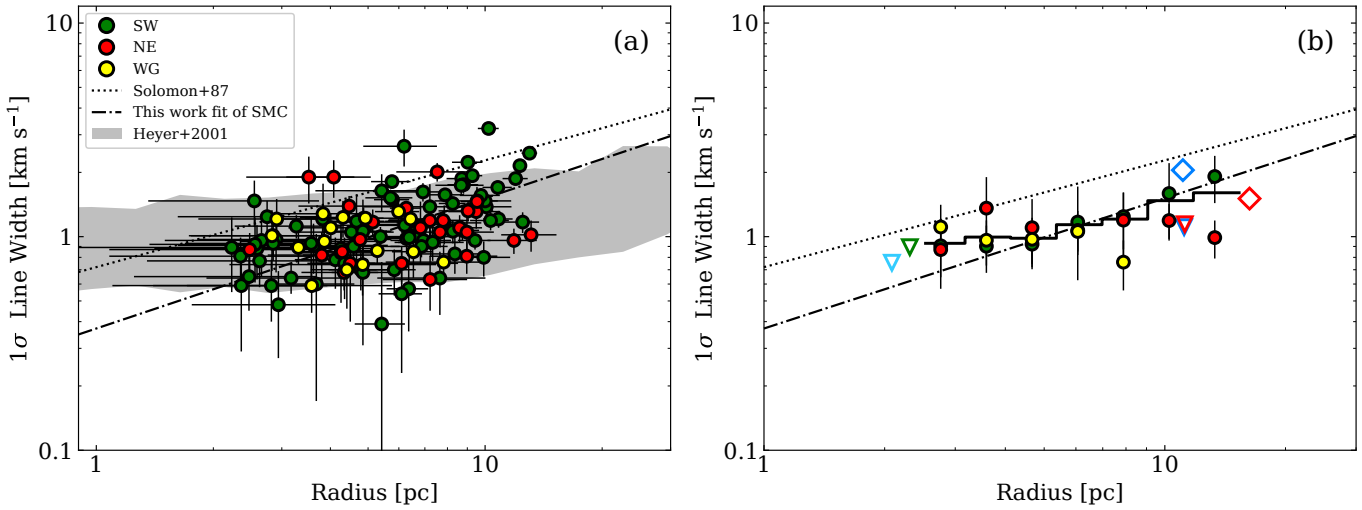

Fig. 5. Size-linewidth relation of SMC clouds. Both parameters at 9 pc resolution were corrected for sensitivity and resolution biases by CPROPS. The SW (SW-Bar, DarkPK) clouds are indicated in green, the NE (NE-Bar, N66) clouds in red, and the WG (N83, NGC 602, N88) clouds in yellow. The black dotted line in both panels indicates the scaling relation for Milky Way GMCs (Solomon et al. 1987). In panel (a), the gray shadow corresponds to the location of the outer Galaxy clouds (Heyer et al. 2001), and the dot-dashed line shows the best fit obtained for the total sample of the well-resolved SMC clouds ($S/N > 5$) with a slope of 0.61 ± 0.25. In panel (b), we show the average velocity dispersion within logarithmic bins of radius (stepped line) and the best fit (dot-dashed line) of panel (a). The average σ_v and R for the NE (red triangle) and SW (red diamond) clouds by Muller et al. (2010) and the average values for the SW (blue diamond) and N83 (blue triangle) clouds by Bolatto et al. (2008) are shown. The green and cyan triangles correspond to median values (∼1–2 pc resolution) taken from SWBarN (Saldaño et al. 2018) and NGC 602 (Fukui et al. 2020), respectively.

Table 3. Measured properties of SMC clouds.

	SMC				
Property	Min	25th	Median	75th	Max
σ_v	0.39	0.85	1.05	1.31	3.21
R	2.23	4.06	5.81	7.98	13.13
$\log(L_{CO})$	1.82	2.48	2.76	3.04	3.84
$\log(M_{vir})$	2.86	3.47	3.82	4.13	5.04
$\log(\Sigma)$	0.98	1.63	1.82	2.02	2.57
$\log(\sigma_v^2/R)$	−1.55	−0.89	−0.70	−0.50	0.05
α_{CO}	2.65	7.72	10.50	15.10	66.85

Notes. Units: R in pc; σ_v in km s^{-1}; L_{CO} in K km s^{-1} pc^2; M_{vir} in $M_\odot$; Σ in $M_\odot$/pc^2, estimated with the M_{vir}; σ_v^2/R in km^2 s^{-2} pc^{-1}; α_{CO} in $M_\odot$ (K km s^{-1} pc^2)$^{-1}$. Values corresponding to well-resolved clouds ($R \gtrsim 2.2$ pc and $S/N \gtrsim 5$).

intersection with their respective uncertainties by means of the bootstrapping technique. These mean values were defined as the best fit of the X–Y relation. In general, N = 1000–2000 is sufficient to achieve the best fit (no changes in the fitted parameter distributions) when the scatter of data is small. We applied this method to determine the correlations of the CO parameters for the well-resolved SMC clouds with $S/N \gtrsim 5$ as well as for the SW, NE, and WG clouds, separately.

4.2.1. The size-linewidth relation

Figure 5a shows the size-linewidth relation (σ_v–R) for the well-resolved SMC clouds with $S/N \gtrsim 5$. Applying the bootstrapping fit method to the σ_v–R relationship, we found that the size–linewidth relation is given by:

$$\log(\sigma_v) = (-0.43 \pm 0.18) + (0.61 \pm 0.25)\log(R), \quad (9)$$

with a Spearman's correlation coefficient of ρ_S = 0.45. The slope of the SMC relationship is similar to that measured by Bolatto et al. (2008) for GMCs of low-metallicity galaxies (including the SMC clouds observed at 6–17 pc resolution), but our fit is slightly offset to smaller linewidths by ∼0.1 dex. The slope of the relationship increases to ∼0.8 ± 0.2 when we include faint clouds with $S/N > 3$ in intensity. This effect in the slope is identical to that found by Wong et al. (2011) for the LMC clouds, showing that the decomposition of CPROPS for fainter clouds affects the size distribution and results in steeper relations with the linewidth. This is a consequence of the considerable uncertainty introduced in the linewidth and radius by CPROPS for faint clouds, as discussed by Rosolowsky & Leroy (2006).

In Fig. 5b, we show the variation of the mean velocity dispersion within logarithmic bins of the radius for the total sample that shows an inclination slightly lower than our best fit for $R > 5$ pc. Our average values are consistent with previous determinations at 10 pc resolution (see Bolatto et al. 2008; Muller et al. 2010). At smaller sizes ($\lesssim$5 pc), the SMC clouds tend to have larger average linewidths than that expected by the trend of bigger SMC clouds, which is consistent with findings at even smaller scales (∼1–2 pc) in the SMC (Saldaño et al. 2018; Muraoka et al. 2017; Fukui et al. 2020) that show tiny clouds having similar or larger linewidths than the inner Milky Way clouds of similar size (see Sect. 5.3). The behavior in the linewidth at different scale sizes may indicate differences in the dynamic states of small clouds and large GMCs (Heyer et al. 2001; Wong et al. 2019).

4.2.2. The luminosity-scaling relations

Figures 6a and b show the good correlation ($\rho_S \simeq 0.7$) of the CO luminosity with the radius and velocity dispersion for the SMC clouds. Applying the bootstrapping fitting method to both luminosity-scaling relations, we found that the best fists are:

$$\log(L_{CO}) = (0.7 \pm 0.2) + (2.7 \pm 0.3)\log(R), \quad (10)$$

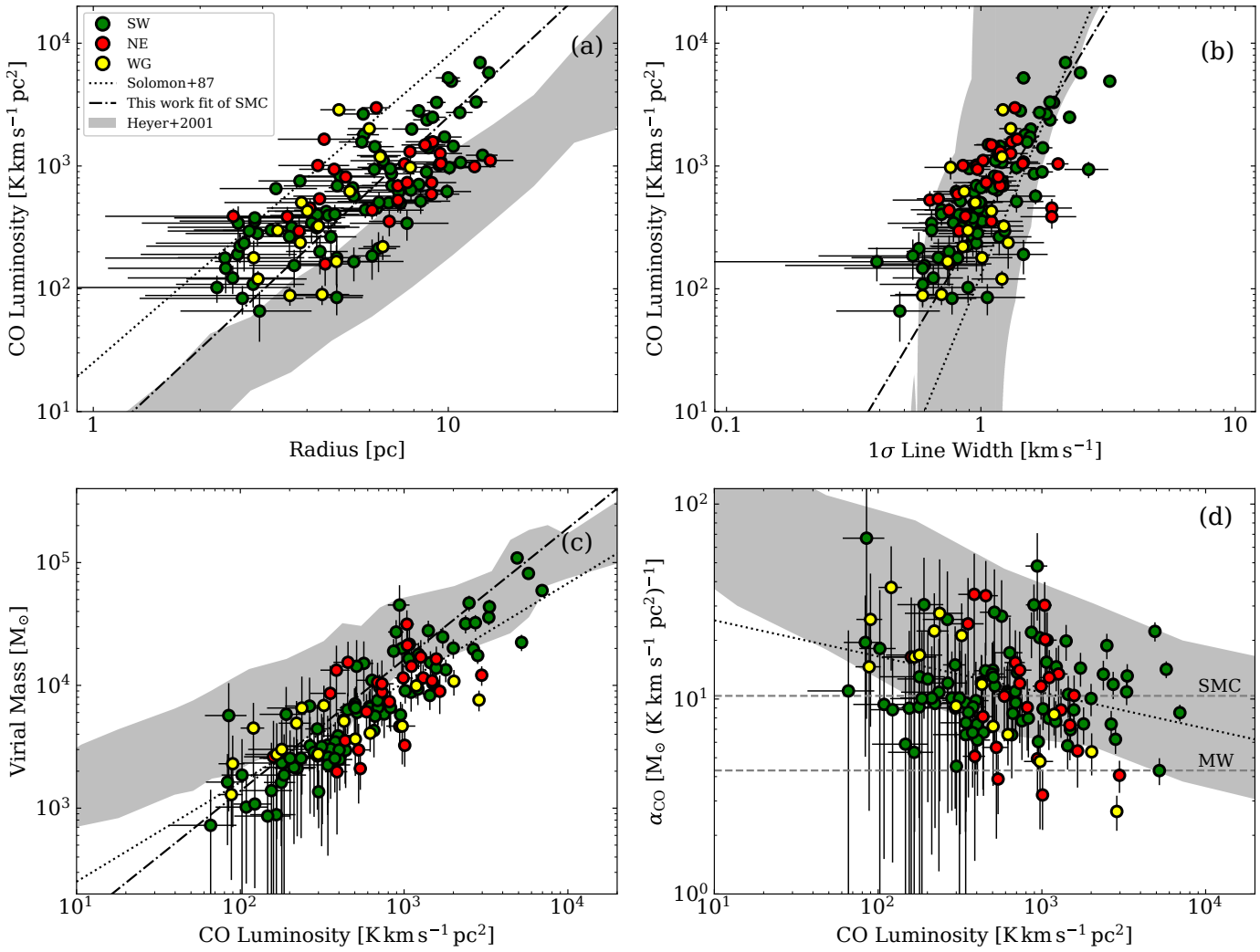

Fig. 6. Scaling relation between luminosity, radius, velocity dispersion, virial mass, and CO-to-H_2 conversion factor for SMC clouds. In all panels, the dotted lines indicate the relations of Solomon et al. (1987), while gray shadows show the location of the outer Galaxy clouds (Heyer et al. 2001). In panels (a), (b), and (c) the dot-dashed lines display the best fit for the whole sample of the SMC ($S/N > 5$ and $R > 2.2$ pc). In panel (d), the median value of $\alpha_{CO} = 10.5 \pm 5\, M_\odot\,(\mathrm{K\,km\,s^{-1}\,pc^2})^{-1}$ for the SMC clouds obtained in this work is shown with a horizontal dashed line. The canonical conversion factor ($\alpha_{CO} = 4.36\, M_\odot\,(\mathrm{K\,km\,s^{-1}\,pc^2})^{-1}$) for the Milky Way (MW in the panel) defined for clouds with $L_{CO} = 10^5$ K km s^{-1} pc^2 is also indicated with a horizontal dashed line.

and

$$\log(L_{CO}) = (2.67 \pm 0.04) + (3.6 \pm 0.3)\log(\sigma_\upsilon). \quad (11)$$

Taking the Milky Way luminosity-scaling relations into account (Eqs. (2) and (3)), the SMC clouds are less luminous than the inner Milky Way clouds of similar size by a factor of ∼3. However, for similar linewidths, the luminosities of the SMC clouds tend to be higher by a factor of ∼3.5. These results are consistent with those found by Bolatto et al. (2008), who indicated that the SMC clouds tend to be underluminous for their sizes and overluminous for their velocity dispersions. Nonetheless, comparing our data with those of the outer Galaxy from Heyer et al. (2001), we found that the SMC clouds tend to be smaller, but as turbulent as those of the outer Galaxy for a given luminosity.

Finally, we did not find considerable differences between the luminosity-scaling relations for the SW, NE, and WG clouds, indicating that the environment in the SMC regions does not affect these scaling relations.

4.2.3. Virial mass - CO luminosity relation

The relationship between M_{vir} and L_{CO} of the SMC clouds is shown in Fig. 6c. The best fit of our data gives the following relation between both parameters:

$$\log(M_{vir}) = (1.0 \pm 0.2) + (1.0 \pm 0.2)\log(L_{CO}). \quad (12)$$

The clouds with high luminosity have similar values as those of the outer Galaxy while those with lower luminosity deviate from this trend, showing lower virial masses and approaching the inner Milky Way GMCs. The larger size and the smaller velocity dispersion of the SMC clouds for a given luminosity, as can be seen in Figs. 6a and b, shift in opposite directions with respect to the Milky Way clouds and approximately cancel out when the virial mass is calculated, giving a strong correlation between M_{vir} and L_{CO} ($\rho_S \simeq 0.85$), and a good agreement among the SMC and inner Milky Way clouds between 10^3 to 10^4 $M_\odot$. The deviation seen between the SMC and outer Galaxy clouds for lower luminosities may be explained by a selection effect in the analysis of Heyer et al. (2001), who excluded the narrow-line regions from the cloud catalog.

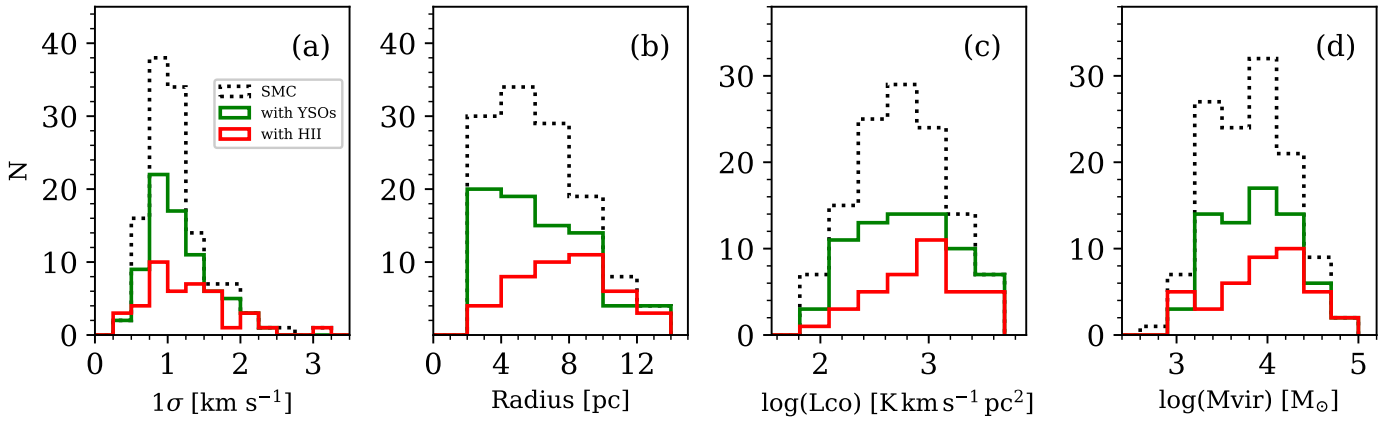

Fig. 7. Histogram of velocity dispersion (a), radius (b), CO luminosity (c), and virial mass (d) of CO clouds of SMC spatially associated with YSOs (green) and HII regions (red). The histograms in dotted lines correspond to the full sample of the SMC (gray histograms in Fig. 4).

As the virial mass increases with $\sigma^2 R$ and L_{CO} are proportional to σR^2, an anticorrelation of the virial mass-based CO-to-H_2 conversion factor ($\alpha_{CO} = M_{vir}/L_{CO}$) with L_{CO} is expected (see Bolatto et al. 2013). In Fig. 6d, we show that the α_{CO}–L_{CO} relationship of the SMC clouds fall within the trend found for the outer Galaxy clouds, which follow $\alpha_{CO} \propto L_{CO}^{-0.5}$ (Heyer et al. 2001). The Milky Way clouds, following $\alpha_{CO} \propto L_{CO}^{-0.2}$, are also shown in the figure. For the SMC, we found a roughly constant $\alpha_{CO} - L_{CO}$ relationship for luminosities between 60 and 5×10^3 K km s^{-1} pc^2, with a slope of -0.20 ± 0.17, and with a Spearman's coefficient of $\rho_S = -0.2$, implying a very weak anticorrelation trend.

We determined the virial mass-based CO-to-H_2 conversion factor for the SMC of $\alpha_{CO(1\text{-}0)} = 10.5\, M_\odot$ (K km s^{-1} pc^2)$^{-1}$ with a standard deviation of $\sim 5\, M_\odot$ (K km s^{-1} pc^2)$^{-1}$. This α_{CO} represents the median value of the conversion factors of the 124 CO clouds based on their virial masses and CO luminosities shown in Table 2. This value is approximately 2.5 times larger than the canonical Galactic value, which was obtained for clouds with typical $L_{CO} = 10^5$ K km s^{-1} pc^2. Our derived SMC value is consistent with the expectation of a higher α_{CO} for Galactic virialized clouds with $L_{CO} \sim 2 \times 10^3$ K km s^{-1} pc^2 (Solomon et al. 1987; Bolatto et al. 2013). We did not find differences between the median conversion factor estimated for the SW, NE, and WG clouds.

4.3. Association of CO clouds with YSOs and HII regions

We inspected the association of the CO clouds with YSOs and HII regions to assess the CO cloud parameters in star-forming regions. We compared the positions of the SMC YSOs and HII regions with the position of the CO clouds in the three studied regions in this work. More details of this comparison are given in Appendix B.

For the YSO-CO cloud association, we used the positions of more than 1000 YSOs identified in the SMC (Simon et al. 2007; Carlson et al. 2011; Sewiło et al. 2013). We required that the position differences between YSOs and CO clouds be less than the deconvolved radius of the clouds.[3] With this criteria, we found that ~43% (76/177) of the CO clouds may be associated with YSOs. We also associated the CO clouds with the HII regions using the 215 HII regions in the main body of the SMC identified by Pellegrini et al. (2012). In this case, we compared the HII position within twice the CO radius, as the HII region may have expanding shells that could affect the nearby environment of the molecular cloud. We found that ~24% (42/177) of the SMC clouds are spatially associated with HII regions in our observed areas. Our analysis also showed that after accounting for the fact that there is some overlap (16% of the clouds are associated with both YSOs and HII regions), about half of the clouds are associated with ongoing star formation (either YSOs or HII regions) but also that close to half of the clouds are not. This is consistent with the findings in other nearby galaxies (e.g., Corbelli et al. 2017).

With the resulting associations, we constructed histograms of the molecular parameters of CO clouds likely associated with YSOs and HII regions, shown in Fig. 7. We plotted the histogram of the SMC total sample for comparison. To quantitatively determine an association, we performed a K-S test on the SMC total sample and the clouds associated with YSOs and HII regions. The K–S result shows that the SMC clouds associated with YSOs have velocity dispersion, radius, CO luminosity, and virial mass similar to the total CO sample of the SMC (p-values > 30%); therefore, they have attributes that are consistent with belonging to the same parent distribution. However, the histograms of the CO clouds associated with HII regions and the total SMC sample yielded p-values $\lesssim 5\%$, suggesting that HII regions are preferentially associated with larger, more luminous, and more massive clouds (Figs. 7b–d).

4.4. The mass distribution of the SMC clouds

For the first time, we have a large number (over 100) of resolved clouds to determine the mass spectrum of the SMC clouds. The mass distribution is used to quantify the characteristics of the populations between systems and gives important parameters for theories and models of star-forming clouds. Instead of using the power-law mass spectrum ($dN/dM \propto M^\beta$), we used the integration of this mass spectrum known as the cumulative mass distribution (CMD), given by a power-law distribution as:

$$N(M' > M) = \left(\frac{M}{M_0}\right)^{\beta+1}. \quad (13)$$

This distribution gives the number of clouds (N) with masses (M') greater than a reference mass (M) as a function of that reference mass. In all known cases, the power-law index β takes

[3] For unresolved clouds without a measured size, a radius of 2.2 pc (the limit of resolved clouds) are assigned.

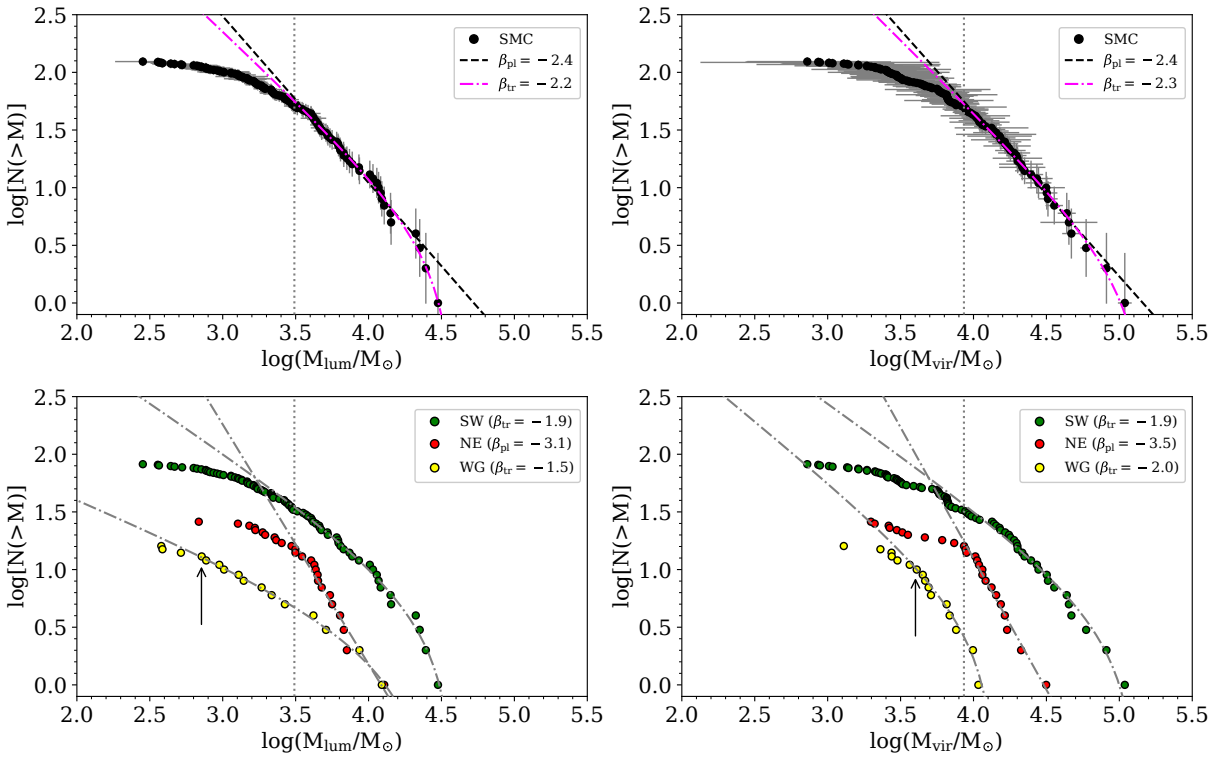

Fig. 8. Top Panels: Cumulative luminous mass distribution (top-left) and cumulative virial mass distribution (top-right) of the SMC clouds (black dots) at 9 pc resolution. In gray bars, the error in both axes is indicated. The vertical dotted line corresponds to the completeness limits ($M_{\rm lum} = 3.1 \times 10^3\,M_\odot$ and $M_{\rm vir} = 8.6 \times 10^3\,M_\odot$) from which the best fit is applied to the SMC spectra. The power-law model best fit ($\beta_{\rm pl} = -2.4$) is shown in black dashed lines, while the truncated model ($\beta_{\rm tr} \simeq -2.2$) best fit is shown with magenta dot-dashed lines. Bottom Panels: The CMD of the SW, NE, and WG clouds are indicated in green, red, and yellow dots, respectively. In gray dot-dashed lines, the best fit of these CMDs is indicated. In the case of the WG clouds, the black arrows indicate the completeness limits ($M_{\rm lum} = 7.15 \times 10^2\,M_\odot$ and $M_{\rm vir} = 4.0 \times 10^3\,M_\odot$).

values lower than −1. In general, in cases where $\beta > -2$, the total galaxy's molecular gas is dominated by massive GMCs, while for steeper distributions with $\beta < -2$, most of the total molecular mass of a galaxy is contained in smaller clouds. The maximum mass in the distribution is represented by M_0, and it generally scales with the total mass of the sample.

The power-law distribution tends to overpredict the number of clouds at very high masses where the mass spectrum can undergo a sharp roll-off with a truncated end at M_0. This feature has been found to be very pronounced in the mass spectrum of the inner disk of the Milky Way (Rosolowsky 2005), in the galactic center of M51 (Colombo et al. 2014), and in M33 (Gratier et al. 2012). To take this feature into account, we considered the truncated CMD given by:

$$N(M' > M) = N_0 \left[\left(\frac{M}{M_0} \right)^{\beta+1} - 1 \right]. \quad (14)$$

In this distribution, N_0 is the number of clouds with masses $> 2^{1/(\beta+1)} M_0$ where the CMD begins to deviate significantly from the power law. For $N_0 \sim 1$, the deviation is negligible.

The advantage of using the CMD as a mass spectrum is that we can generate the mass distribution without choosing a bin size that would introduce some bias in the estimation of the main parameters of Eqs. (13) and (14), (Rosolowsky 2005). We used the methodology described in Rosolowsky (2005) by using the IDL program provided by this author (private communication). The algorithm uses the "error-in-variables" method that maximizes the likelihood of an $\{M, N\}$ data set (with associated uncertainties) modeled with parameters $\{N_0, M_0, \beta\}$. We determined these parameters for the luminous mass distribution ($M_{\rm lum}$ from Eq. (8)) and for the virial mass distribution ($M_{\rm vir}$ from Eq. (7)). In Fig. 8, the CMD for both luminous and virial mass of the 124 SMC clouds ($S/N > 5$ and $R > 2.2$ pc) are shown. The fit of the cumulative luminous mass distribution was performed above the completeness limit of $M_{\rm lum} \simeq 3.1 \times 10^3\,M_\odot$. For the cumulative virial mass distribution, the completeness limit is $M_{\rm vir} \simeq 9.0 \times 10^3\,M_\odot$. Both the luminous and the virial mass distribution include 50 clouds above the completeness limits. In Table 4, the parameters of the best fit of the power law and the truncated models and the number of clouds used for the fit are indicated, and we also include the best fits for the SW, NE, and WG regions, all of which are also shown in Fig. 8. As they have very low numbers of clouds and thus suffer from uncertainties in the CMDs, we have not included these fits in our analysis.

The best fit for the SMC mass spectra gave power indexes of $\beta < -2$. This indicates that the molecular gas in the SMC is preferentially distributed in low-mass clouds. The cumulative luminous mass distribution of the SMC shows a moderated truncation in the high-mass end with $N_0 = 3.0 \pm 3.0$ and a maximum mass of $M_0 = (3.8 \pm 0.9) \times 10^4\,M_\odot$. While for the cumulative virial mass distribution, the truncation is negligible, with $N_0 = 1.3 \pm 1.0$ and a higher maximum mass of $M_0 = (15.8 \pm 5.0) \times 10^4\,M_\odot$. Therefore, rather than following a truncated model, the cumulative virial mass distribution follows a power-law distribution (within the errors) beyond the completeness limit. We found that the CMD for the SMC is similar to those obtained in the nearest irregular galaxy LMC by Wong et al. (2011) except that the maximum mass M_0 in both

Table 4. Best fit of the CMDs for the SMC clouds.

Luminous mass distribution					
Region	Model	β	M_0 ($10^4\,M_\odot$)	N_0	N[(a)]
SMC	PLaw	-2.4 ± 0.2	5.3 ± 1.5	–	50
SMC	Trunc.	-2.2 ± 0.3	3.8 ± 0.9	3.0 ± 3.0	50
SW	Trunc.	-1.9 ± 0.3	3.8 ± 0.8	4.5 ± 4.0	32
NE	PLaw	-3.1 ± 0.6	1.2 ± 0.3	–	15
WG[(b)]	Trunc.	-1.5 ± 0.3	2.6 ± 1.3	2.3 ± 2.0	13
Virial mass distribution					
Region	Model	β	M_0 ($10^4\,M_\odot$)	N_0	N[(a)]
SMC	PLaw	-2.4 ± 0.2	14.5 ± 4.2	–	50
SMC	Trunc.	-2.3 ± 0.2	15.5 ± 5.8	1.4 ± 1.0	50
SW	Trunc.	-1.9 ± 0.3	13.3 ± 4.0	3.4 ± 3.0	32
NE	PLaw	-3.3 ± 0.5	3.0 ± 2.1	–	15
WG[(b)]	Trunc.	-2.0 ± 0.2	1.4 ± 1.0	3.7 ± 2.0	10

Notes. The best fit of the power law (PLaw) and truncated (Trunc.) models for the SMC clouds are given. In the case of the SW, NE, and WG regions, only the models that best fit the CMDs are indicated. The fitting was performed above the completeness limit of $M_{\rm lum} = 3.1 \times 10^3\,M_\odot$ and $M_{\rm vir} = 8.6 \times 10^3\,M_\odot$ for all regions. [(a)]The last column indicates the number of well-resolved clouds with $S/N > 5$ used for the fit. [(b)]For the WG region, the completeness limits are $M_{\rm lum} = 7.15 \times 10^2\,M_\odot$ and $M_{\rm vir} = 4 \times 10^3\,M_\odot$.

luminous and virial mass distributions for the SMC are about one order of magnitude lower than those of the LMC.

The power indexes of the CMDs found in the SMC are also generally consistent with those estimated for galaxies with nonspiral morphology, for example, the irregular LMC galaxy ($\beta \simeq -2.3$, Wong et al. 2011) and the lenticular galaxy NGC 4526 ($\beta \simeq -2.4$, Utomo et al. 2015), or those of galaxies in more quiescent environments beyond the galactic center of spiral galaxies, such as M33 ($\beta = -2.3$, Gratier et al. 2012), M51 ($\beta \simeq -2.5$, Colombo et al. 2014), and the outer Milky Way ($\beta = -2.5$, Rosolowsky 2005). However, shallower CMDs ($\beta > -2.0$) are found toward the center of these galaxies (Rosolowsky 2005; Braine et al. 2018).

As we detail in Sect. 5, the SMC clouds tend to be in virial equilibrium, so the virial mass values represent the total gas mass of the clouds, suggesting that the virial mass distribution would be a good representation of the real CMD of the SMC. In this scenario, the SMC would be dominated by low-mass clouds across the galaxy (within uncertainties), unlike spiral galaxies.

5. Discussion

5.1. The stability of the SMC clouds

We analyzed the dynamical state of the SMC clouds plotting the σ_v^2/R ratio as a function of the surface density $\Sigma = M_{\rm gas}/\pi R^2$, where σ_v is the velocity dispersion, R is the (deconvolved) radius, and $M_{\rm gas}$ is the total gas mass of the cloud. This relationship is shown in panel (a) of Fig. 9 for the 124 well-resolved and high S/N CO clouds identified in this work. We used the Galactic conversion factor to estimate the surface densities of these CO clouds. Their Σ range from 5 to $160\,M_\odot\,{\rm pc}^{-2}$. For the assumed conversion factor, most of the CO clouds are close to the marginally gravitationally bound line. If we had used a larger conversion factor, as is expected in low-metallicity galaxies (Leroy et al. 2011; Jameson et al. 2018), the luminous CO mass would be greater and the CO clouds would move to the right in the plot, becoming more strongly bound.

For an alternative result independent of conversion factor assumptions, we examined the stability of the molecular clouds identified by Takekoshi et al. (2017) in the 1.1 mm survey of the SMC at 12 pc resolution using their estimated dust-based masses. Takekoshi et al. (2017) estimated cloud gas masses by fitting the FIR spectral energy distribution (SED) with a modified black body model that used a dust emissivity index of $\beta = 1.2$ and GDR= 1000. Within our observed area, there are 19 dust clouds with reliable deconvolved radii in the range ~5–40 pc (see Table 2 of Takekoshi et al. 2017).

To estimate the velocity dispersion of these 19 clouds, we used an "equivalent linewidth" ($\sigma_{v,\rm eq}$) following the method by Heyer et al. (2001),

$$\sigma_{v,\rm eq} = \frac{I_{\rm CO}}{\sqrt{2\pi}\,T_{\rm peak}}, \tag{15}$$

where $I_{\rm CO}$ is the CO intensity and $T_{\rm peak}$ is the peak temperature measure within the dust clouds. We determined both $I_{\rm CO}$ and $T_{\rm peak}$ by convolving the CO APEX of 30″ (9 pc) resolution to the 1.1 mm data resolution of 40″ (12 pc). Then, we obtained the integrated CO spectrum over the area of the dust cloud as defined by Takekoshi et al. (2017). We used this method because it is less sensitive to broad line wings or the presence of multiple CO cloud components along the line of sight than a moment-based measurement, and it requires no assumption about the line shape (unlike fitting the integrated CO spectrum, Leroy et al. 2016). We found $\sigma_{v,\rm eq}$ is roughly similar to the line width of the brightest CO component in the line of sight.

As Fig. 9a shows, most of the dust-identified clouds are close to the gravitational virial equilibrium. The dynamic range for Σ is small, from ~60 to 160 $M_\odot\,{\rm pc}^{-2}$, but this is likely a limitation of the dust observations. We list the parameters of the dust clouds in Table 5.

In Fig. 9b, we show the virial parameter ($\alpha_{\rm vir}$) for the 19 dust-identified SMC clouds as a function of their total gas mass ($M_{\rm gas}$). We computed the virial parameter as $\alpha_{\rm vir} = M_{\rm vir}/M_{\rm gas}$, where $M_{\rm vir}$ is from Eq. (7) and uses the equivalent linewidth and the deconvolved radius of dust clouds and $M_{\rm gas}$ is the total gas mass measured by Takekoshi et al. (2017). We estimated an $\alpha_{\rm vir}$ within ±0.3 dex of unity for most clouds, although the full range is $\alpha_{\rm vir} \sim 0.4$–4. The average virial parameter for these SMC clouds is $\alpha_{\rm vir} = 1.1^{+1.2}_{-0.3}$, which is in very good agreement with virial equilibrium within the errors. This suggests that any support by a magnetic field plays a secondary role in the cloud equilibrium, in good agreement with recent measurements of the SMC magnetic fields (Lobo Gomes et al. 2015; Kaczmarek et al. 2017), which are too low to provide significant support (Bot et al. 2007).

Some considerations and caveats regarding our analysis must be stated. First, in the calculation of $\Sigma_{\rm gas}$, Takekoshi et al. (2017) used GDR = 1000 to determine the gas mass. Roman-Duval et al. (2014) recommended GDR ~1800 with a ±0.3 dex uncertainty. Roman-Duval et al. (2017) found that the GDR is a function of surface density, with a factor of seven change over $\Sigma_{\rm gas} \sim 10$–$100\,M_\odot\,{\rm pc}^{-2}$ in the direction of lower values in the denser ISM, although with significant methodological uncertainties. The GDR = 1000 value is in good agreement with their Fig. 14b for $\Sigma_{\rm gas} \sim 100\,M_\odot\,{\rm pc}^{-2}$, but it is possible that the

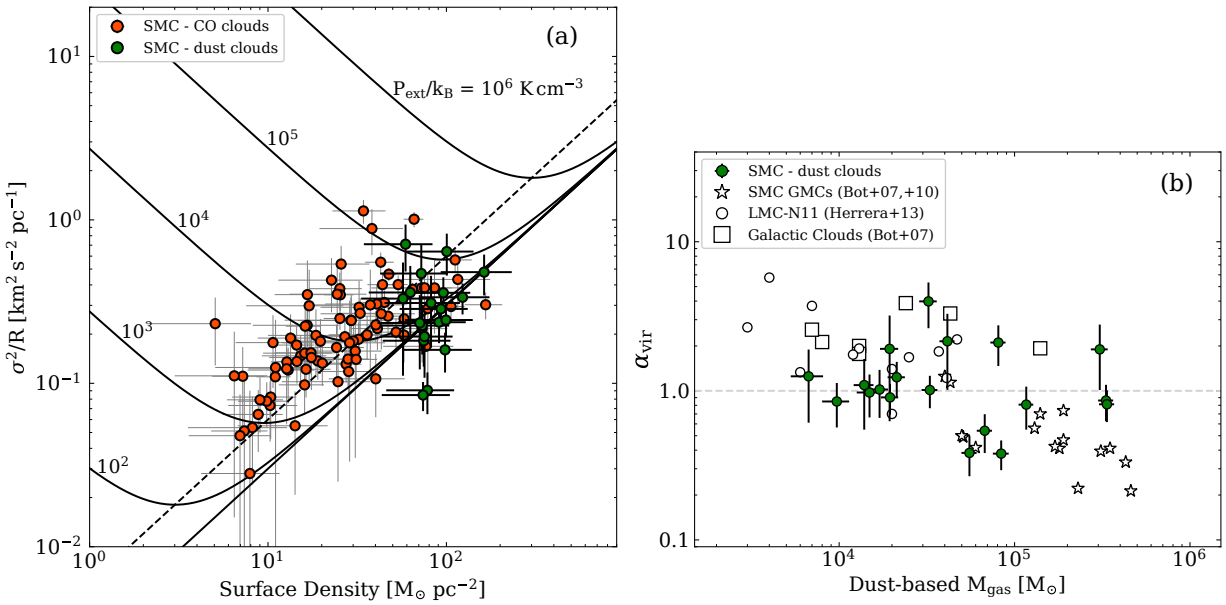

Fig. 9. Panel (a): $\Sigma - \sigma_v^2/R$ relationship for the SMC clouds. The red dots show the CO clouds of this work, whose Σ was calculated from their luminous mass assuming the Galactic conversion factor. The green dots correspond to the dust clouds identified by Takekoshi et al. (2017) at 12 pc resolution. Their Σ were calculated from the dust-based total gas mass by these authors and the velocity dispersion by mean Eq. (15). The black curves indicate gravitational virial conditions for clouds confined by external pressures from $P_{ext}/k_B = 10^2$ to 10^6 K cm^{-3}. The straight solid line corresponds to virialized clouds without pressure, and the dashed line is the marginal gravitationally bound condition (identical kinetic and gravitational energy). Panel (b): birial parameter (α_{vir}) vs. dust-based total gas mass for the same SMC dust clouds shown in panel (a). We have added for comparison the virial parameters of the Milky Way (squares) and SMC GMCs (star symbols) from Bot et al. (2007, 2010), and the LMC GMCs (empty circles) from Herrera et al. (2013). The average virial parameter for the SMC dust clouds is $\alpha_{vir} = 1.1^{+1.2}_{-0.3}$.

Table 5. Physical parameters for SMC dust clouds from Takekoshi et al. (2017) within our observed regions.

ID [a]	σ_v [b] (km s^{-1})	R_{deconv} [c] (pc)	L_{CO} [d] (caption)	M_{vir} ($10^3 M_\odot$)	M_{gas} [c] ($10^3 M_\odot$)	Σ_{gas} ($M_\odot$ pc^{-2})	α_{vir} [e] –	α_{CO} [f] (caption)
SW-1	2.8 ± 0.2	34.1 ± 6.8	111.0 ± 45.1	278.0 ± 68.2	332.1 ± 32.7	90.9 ± 37.3	0.8 ± 0.2	29.9 ± 12.5
SW-2	2.8 ± 0.1	32.8 ± 6.6	89.4 ± 35.8	267.4 ± 57.1	336.1 ± 33.2	99.4 ± 41.2	0.8 ± 0.2	37.6 ± 15.5
SW-3	3.2 ± 0.3	16.0 ± 3.2	56.7 ± 23.3	170.4 ± 46.7	80.8 ± 8.0	100.5 ± 41.4	2.1 ± 0.6	14.3 ± 6.0
SW-4	1.5 ± 0.1	14.8 ± 3.0	47.1 ± 19.3	34.6 ± 8.4	67.6 ± 6.7	98.2 ± 41.0	0.5 ± 0.1	14.4 ± 6.1
SW-5	1.2 ± 0.1	15.0 ± 3.0	8.3 ± 3.3	22.5 ± 5.9	55.3 ± 5.5	78.2 ± 32.2	0.4 ± 0.1	66.6 ± 27.3
SW-6	1.4 ± 0.2	8.6 ± 1.7	5.7 ± 2.3	17.5 ± 6.1	17.0 ± 2.0	73.2 ± 30.2	1.0 ± 0.4	29.8 ± 12.5
SW-7	1.7 ± 0.1	10.6 ± 2.1	14.8 ± 5.9	31.9 ± 7.4	32.9 ± 3.4	93.2 ± 38.2	1.0 ± 0.2	22.2 ± 9.2
SW-9	2.5 ± 0.6	13.5 ± 2.7	9.7 ± 4.1	87.8 ± 45.7	41.4 ± 4.1	72.3 ± 29.8	2.1 ± 1.1	42.7 ± 18.5
SW-20	1.6 ± 0.2	5.4 ± 1.1	5.1 ± 2.0	14.4 ± 4.6	14.9 ± 2.3	162.6 ± 70.9	1.0 ± 0.3	29.2 ± 12.3
SW-22	1.4 ± 0.3	7.9 ± 1.6	4.5 ± 2.0	16.1 ± 7.6	13.9 ± 1.8	70.9 ± 30.1	1.2 ± 0.6	30.9 ± 14.3
NE-1	3.8 ± 0.8	39.4 ± 7.9	80.1 ± 33.9	591.7 ± 275.9	305.9 ± 33.7	62.7 ± 26.1	1.9 ± 0.9	38.2 ± 16.7
NE-2	3.1 ± 0.4	13.2 ± 2.6	15.0 ± 6.1	131.9 ± 42.8	32.3 ± 3.7	59.0 ± 24.2	4.1 ± 1.4	21.5 ± 9.1
NE-3	1.7 ± 0.1	8.4 ± 1.7	10.6 ± 4.2	25.2 ± 5.9	21.3 ± 2.4	96.1 ± 40.4	1.2 ± 0.3	20.1 ± 8.3
NE-4	1.9 ± 0.6	10.4 ± 2.1	3.2 ± 1.4	39.0 ± 25.9	19.4 ± 2.3	57.1 ± 24.0	2.0 ± 1.4	60.6 ± 27.5
NE-6	2.0 ± 0.2	22.3 ± 4.5	32.9 ± 13.3	92.8 ± 26.4	116.6 ± 11.2	74.6 ± 31.0	0.8 ± 0.2	35.4 ± 14.7
NE-12	1.3 ± 0.3	5.1 ± 1.0	3.0 ± 1.3	9.0 ± 4.5	6.7 ± 1.4	82.0 ± 36.4	1.3 ± 0.7	22.3 ± 10.7
Wing-2	1.3 ± 0.0	19.0 ± 3.8	38.8 ± 15.5	33.4 ± 6.8	83.9 ± 8.7	74.0 ± 30.6	0.4 ± 0.1	21.6 ± 8.9
Wing-4	1.5 ± 0.1	7.1 ± 1.4	8.7 ± 3.5	16.6 ± 3.5	19.5 ± 2.2	123.1 ± 50.5	0.9 ± 0.2	22.4 ± 9.4
N88	1.1 ± 0.2	6.4 ± 1.3	6.4 ± 2.7	8.1 ± 3.4	9.7 ± 1.7	75.4 ± 33.4	0.8 ± 0.4	15.2 ± 6.9

Notes. [a]Identification (ID) from Takekoshi et al. (2017). [b]Equivalent linewidth from Eq. (15). [c]The deconvolved radius (R_{deconv}) and total gas mass (M_{gas}) from Takekoshi et al. (2017). We assume an uncertainty of 20% in R. [d]L_{CO} is in unit of 10^2 K km s^{-1} pc^2 [e]Virial parameter $\alpha_{vir} = M_{vir}/M_{gas}$. [f] α_{CO} based on total gas mass (M_{gas} of Col. 6), in unit of $M_\odot$ (K km s^{-1} pc^2)$^{-1}$.

true GDR is larger, which would cause the dust clouds to be more bound.

Second, Takekoshi et al. (2017) adopted a fixed dust emissivity index $\beta = 1.2$ in the SED fit and the dust emissivity can have a large impact on the dust-based total gas mass determination. Typically, the dust emissivity follows a power law with the wavelength ($\kappa \propto \lambda^{-\beta}$) and with power indexes (β) between one and two. However, the dust emissivity is also a function of the dust

grain properties determined by coagulation, density, and temperature (Ossenkopf & Henning 1994; Bot et al. 2010; Paradis et al. 2011). The study done by Roman-Duval et al. (2017) analyzes the dust emissivity and GDR in the SMC, and the authors found that matching depletion measurements may require reducing the GDR, although this could also be explained by biases in the UV absorption spectroscopy used to determine depletions introduced by the complex SMC velocity structure and also possibly Milky Way confusion. Adjustments in the direction of lower GDR would drive SMC dust clouds toward lower surface densities, increasing their virial parameter.

Third, another caveat in our determinations is the fact that there may be several CO clouds along the line of sight to a dust cloud, all of which would be included in our velocity dispersion calculation despite the fact that some may be chance alignments. This would artificially increase the velocity dispersion of the integrated spectrum associated with the dust cloud and consequently its virial mass as well. The inclusion of multiple velocity components would be correct if a dust cloud has a number of CO-emitting cores surrounded by a CO-faint envelope, but if some of these objects are not gravitationally associated, we could overestimate the resulting virial mass. In addition, correction for such an effect could drive some clouds to lower virial parameters.

5.2. CO-to-H_2 conversion factor in the SMC

Under the assumption of virial equilibrium, we can estimate the CO-to-H_2 conversion factor for the SMC through the $\alpha_{\rm CO}^{\rm vir} = M_{\rm vir}/L_{\rm CO}$ ratio. In Sect. 4.2.3, we found that this conversion factor is roughly constant with the luminosity for the SMC CO clouds (see Fig. 6) identified by CPROPS. We determined a median value of $\alpha_{\rm CO}^{\rm vir} \sim 10.5 \pm 5\,M_\odot\,({\rm K\,km\,s^{-1}\,pc^2})^{-1}$ at 9 parsec resolution, approximately 2.5 times the canonical $\alpha_{\rm CO}$ value in the inner disk of the Milky Way ($4.36\,M_\odot\,({\rm K\,km\,s^{-1}\,pc^2})^{-1}$, Bolatto et al. 2013).

This value of the conversion factor for the SMC CO clouds is consistent with other virial mass-based conversion factors of ≈6–17 $M_\odot\,({\rm K\,km\,s^{-1}\,pc^2})^{-1}$ calculated across the Magellanic Clouds at similar resolution (Bolatto et al. 2003, 2008; Herrera et al. 2013; Muraoka et al. 2017) and almost two to ten times lower than those obtained using a similar method but at coarser spatial resolution (Rubio et al. 1991, 1993a; Mizuno et al. 2001; Muller et al. 2010). In fact, Rubio et al. (1993a) observed that the conversion factor decreases with the cloud radius, approximately as $\alpha_{\rm CO} \propto R^{0.7}$. As the median radius of the SMC clouds examined in this paper is 5.8 pc (Table 3), a conversion factor of $\sim 13\,M_\odot\,({\rm K\,km\,s^{-1}\,pc^2})^{-1}$ is predicted for the SMC by the Rubio et al. (1993a) relationship, which is consistent to our measurement. On smaller spatial scales, we would expect the SMC $\alpha_{\rm CO}$ to decrease to a smaller value, similar to that of the Milky Way, as we zoom into the CO-emitting core of a cloud. Observations of CO with spatial resolutions of ∼1 pc, which can be easily reached by the ALMA telescope, are required. However, recent ALMA studies of the SMC at such spatial scales (∼0.4–1.0 pc, Saldaño et al. 2018; Valdivia-Mena et al. 2020; Kalari et al. 2020) show a virial mass-based conversion factor in the SMC and Magellanic Bridge similar to the one derived in this study. This result suggests that $\alpha_{\rm CO}$ in the SMC may have reached a constant value independent of the spatial resolution, thus reflecting a conversion factor intrinsic to individual clumpy clouds.

We estimated the CO-to-H_2 conversion factor using the gas mass determination from the dust emission of the CO clouds at 12 pc resolution by equation: $\alpha_{\rm CO}^{\rm dust} = M_{\rm H_2}/L_{\rm CO}$, where $M_{\rm H_2} = M_{\rm gas} - M_{\rm HI}$. For this estimate, we assumed that the molecular component dominates the dust-based total gas mass over the atomic HI gas in the innermost part of the clouds. This assumption is consistent with PDR models of molecular clouds and supported by the results by Jameson et al. (2018) who found that the HI gas only contributes ≲5% to the [CII] emission toward molecular regions in the SMC. Thus, the dust-based conversion factor $\alpha_{\rm CO}^{\rm dust}$ (as an upper limit) is roughly equal to $M_{\rm gas}/L_{\rm CO}$, where the gas mass is taken from Takekoshi et al. (2017) and the CO luminosity is calculated by $L_{\rm CO} = \pi R^2\,I_{\rm CO}$. Here, R is the radius of the dust emission and $I_{\rm CO}$ is the CO intensity used in Eq. (15) and measured in the CO APEX data convolved to 40″ (12 pc) resolution. We obtained a median dust-based $\alpha_{\rm CO}^{\rm dust} = 28 \pm 15\,M_\odot\,({\rm K\,km\,s^{-1}\,pc^2})^{-1}$. This $\alpha_{\rm CO}^{\rm dust}$ is about 6.5 times larger than the typical Milky Way disk conversion factor of $\alpha_{\rm CO} = 4.36\,M_\odot\,({\rm K\,km\,s^{-1}\,pc^2})^{-1}$ (Bolatto et al. 2013).

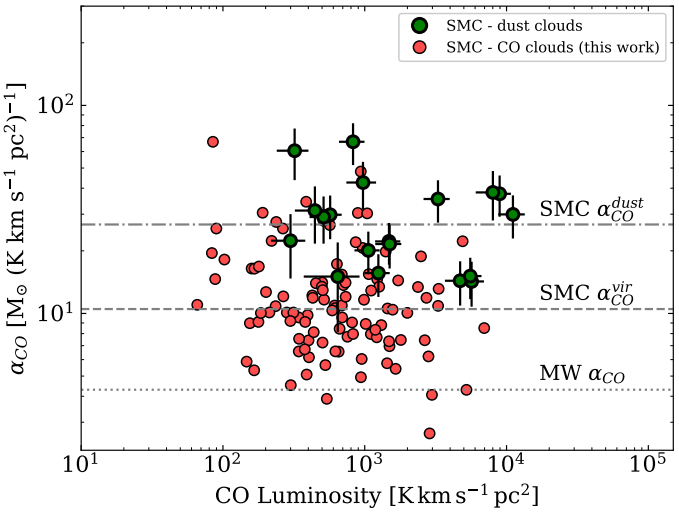

Fig. 10. CO-to-H_2 conversion factor ($\alpha_{\rm CO}$) as a function of the CO luminosity for the 19 dust clouds (green dots) from Takekoshi et al. (2017) within our observed regions at 12 pc resolution. To calculate the CO luminosity, we use the measured CO intensity used in Eq. (15) and the dust cloud size (R) given by Takekoshi et al. (2017). The dot-dashed line indicates the median dust-based $\alpha_{\rm CO}^{\rm dust} = 28 \pm 15\,M_\odot\,({\rm K\,km\,s^{-1}\,pc^2})^{-1}$ for the SMC dust clouds. The conversion factor obtained for each of the 124 SMC CO clouds assuming gravitational virial condition are shown as red dots (see Fig. 6d), with a median value of $\alpha_{\rm CO}^{\rm vir} = 10.5 \pm 5\,M_\odot\,({\rm K\,km\,s^{-1}\,pc^2})^{-1}$ (dashed line). The dotted line corresponds to the canonical Milky Way (MW) conversion factor.

Figure 10 shows the virial mass- and the dust-based conversion factors as a function of the CO luminosity. The dust-based conversion factor $\alpha_{\rm CO}^{\rm dust}$ estimated at 12 pc resolution for the SMC dust clouds lie above the median value derived from the virial method $\alpha_{\rm CO}^{\rm vir}$ for the 124 CO clouds at 9 pc resolution identified by CPROPS. There is no obvious trend of $\alpha_{\rm CO}^{\rm dust}$ or $\alpha_{\rm CO}^{\rm vir}$ with CO luminosity.

We note that since the virial parameter of the dust clouds is close to unity, $\alpha_{\rm vir} \sim 1$ (Fig. 9b), the virial mass on these scales is similar to the mass we obtained from dust. In other words, the $\alpha_{\rm CO}^{\rm dust}$ estimated on 12 pc scales is larger than the $\alpha_{\rm CO}^{\rm vir}$ on 9 pc scales. We refer to the $\alpha_{\rm CO}$ on 12 pc scales as the "dust value" and that at 9 pc scales as the "virial value", as the latter was obtained only through the virial estimate. This estimation of the dust-based conversion factor for the SMC clouds is consistent with previous calculations that used dust or [CII] emission in the SMC (Leroy et al. 2011; Pineda et al. 2017; Jameson et al. 2016, 2018).

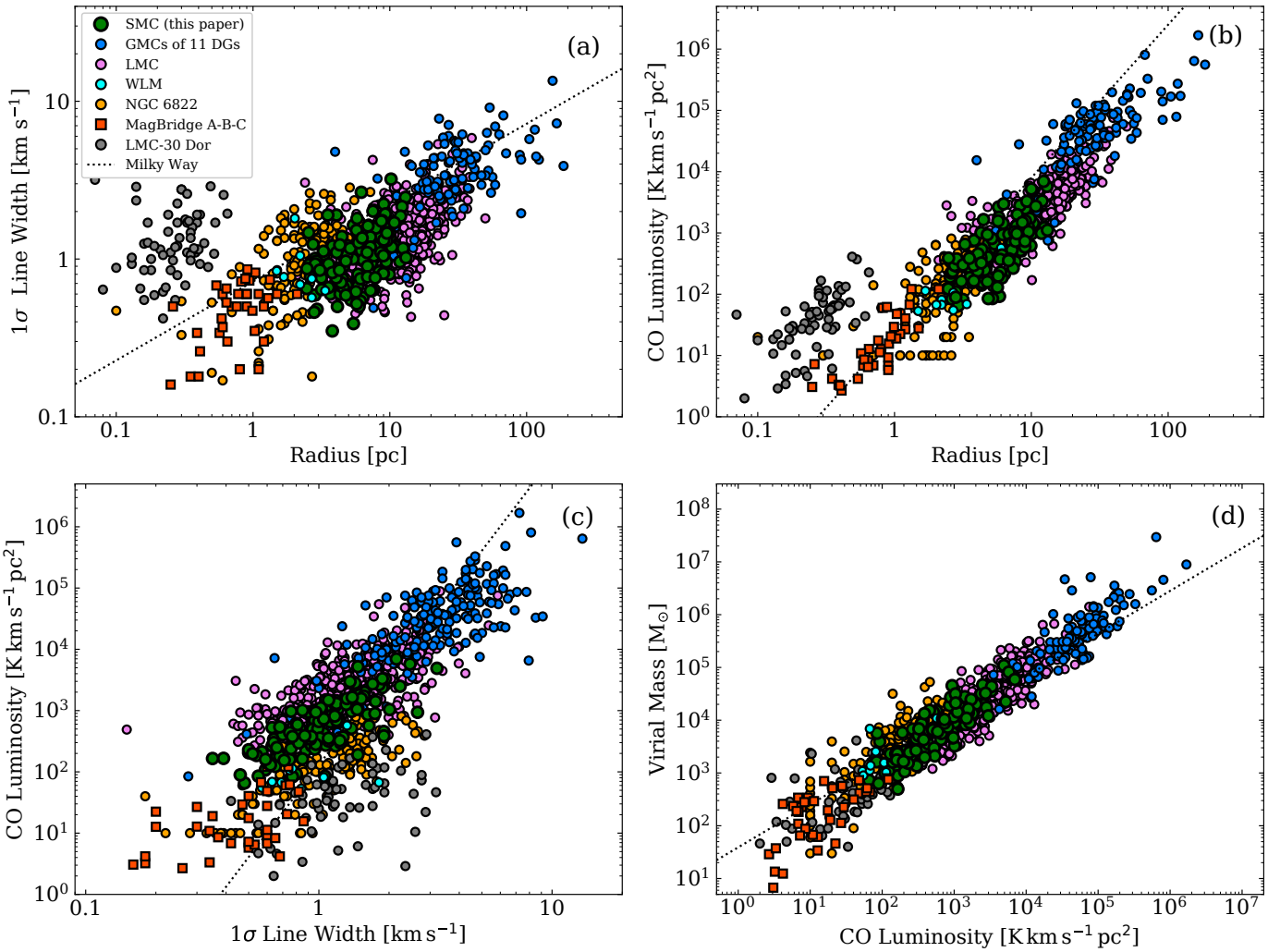

Fig. 11. Scaling relation between the velocity dispersion, radius, luminosity, and virial mass of CO clouds from different low-metallicity galaxies. The SMC clouds (9 pc resolution), indicated in green dots, are compared with the GMCs from 11 Dwarf Galaxies (DGs) at ~6–110 pc resolutions (Bolatto et al. 2008); and the clouds from LMC (11 pc resolution, Wong et al. 2011); WLM (~5 pc, Rubio et al. 2015); NGC 6822 (~2 pc, Schruba et al. 2017); the Magellanic-Bridge A, B, and C (~1 pc, Saldaño et al. 2018; Kalari et al. 2020; Valdivia-Mena et al. 2020); and LMC-30 Doradus (~0.45 pc, Indebetouw et al. 2013). In this figure, we include all SMC clouds with $S/N > 3$. The dotted lines indicate the relations of Solomon et al. (1987) for Milky Way GMCs.

The difference between the two values of α_{CO} may be due to uncertainties in the calculation, which are large. Alternatively, it is possible that the CO-emitting cores of molecular clouds are surrounded by a large envelope of CO-faint gas. In such a scenario, the α_{CO} measured at 9 pc reflects the mass-to-light ratio of the CO core and the material immediately surrounding it, while the measurement at 12 pc resolution is closer to the mass-to-light ratio of the core plus the envelope. Based on this interpretation, the total molecular gas mass of the core could be estimated using $M_{mol} = L_{CO}\,\alpha_{CO}^{vir}$, and the mass of the total core plus the envelope would correspond to $M_{mol} = L_{CO}\,\alpha_{CO}^{dust}$, where the total luminosity of $L_{CO} \simeq 1.9 \times 10^5$ K km s^{-1} pc^2 was measured from cubes for $S/N > 3$. Thus, the core mass and the core plus the envelope mass estimated by these methods are 2.0×10^6 $M_\odot$ and 5.3×10^6 $M_\odot$, respectively.

5.3. Scaling relation of low-metallicity galaxies

We compared the cloud properties that we measured for the SMC with those measured in several low-metallicity galaxies, such as the LMC at 11 pc resolution (Wong et al. 2011), 30 Doradus at 0.45 pc resolution (Indebetouw et al. 2013), WLM at ~5 pc resolution (Rubio et al. 2015), NGC 6822 at ~2 pc resolution (Schruba et al. 2017), and the Magellanic Bridge regions at ~1 pc resolution (Saldaño et al. 2018; Kalari et al. 2020; Valdivia-Mena et al. 2020). These CO observations were done in the $J = 1{-}0$ and $J = 2{-}1$ transitions and analyzed using the CPROPS algorithm (with exception of WLM). The uniformity in the data set, method, and analysis technique was very important for homogeneously comparing molecular properties in different environments. We also used the results of Bolatto et al. (2008), which span resolutions from 6 to 110 pc and identify GMCs in different low-metallicity galaxies with CPROPS. The scaling relations between the velocity dispersion, radius, luminosity, and virial mass of CO clouds from different low-metallicity galaxies are shown in Fig. 11.

An overall feature can be observed in the size-linewidth relation for the low-metallicity galaxies: a departure to lower velocity dispersion (by a factor of approximately two for the SMC clouds) with respect to Milky Way clouds of similar size, although clouds in NGC 6822 appear to better correspond to the

Galactic relation (see Schruba et al. 2017). The departure could be a consequence of CO cloudlets not tracing the total turbulence of large H_2 envelopes, as proposed by Bolatto et al. (2008). This explanation was confirmed by the low value of CO-to-[CII] ratios (∼1/5 the fiducial value for the Milky Way) in the SMC at low A_V (Jameson et al. 2018), suggesting that there is a reservoir of H_2 gas mostly traced by [CII] emission (∼60–70% of the molecular gas, Requena-Torres et al. 2016; Jameson et al. 2018) rather than CO. The best tracer of these "faint-CO" clouds at the edge of the molecular clouds is the [CII] 158 µm emission since the lack of dust shielding allows the UV radiation field to dissociate the CO gas and most of the carbon is in the form of C^+.

Alternatively, the shift in the velocity dispersion of SMC clouds could be due to a deficit of turbulent kinetic energy in the molecular clouds, and thus other sources of energy (e.g., magnetic fields) would be required to support the CO clouds (Bot et al. 2007). However, the gravitational virial equilibrium for the SMC clouds shown in Sect. 5.1 indicates that there is no need for another physical component to keep the SMC clouds bound. Yet, Braine et al. (2018) noted that the low-metallicity could also shift the size-linewidth relation to lower velocity dispersion in GMCs, but they do not distinguish whether the turbulent deficiency is due to changes in the metallicity or in the stellar surface density. This last scenario may be supported by numerical simulations (Hocuk & Spaans 2010), that show that the fragmentation and the turbulence of a cloud (4 pc scale) can decay while the metallicity decreases.

At sub-parsec scales, the scatter in the linewidth increases considerably and may change significantly from region to region. In a quiescent region, such as those in the Magellanic-Bridge (Saldaño et al. 2018; Valdivia-Mena et al. 2020; Kalari et al. 2020), σ_v is between ∼0.2–0.8 km s^{-1}, while in the active 30 Doradus region (Indebetouw et al. 2013) the velocity dispersion is between ∼0.8–5 km s^{-1}. The large linewidths observed in 30 Doradus are suggestive of high stellar feedback and gravity-driven motions in high column density structures (Wong et al. 2019). High linewidths with respect to Milky Way clouds for a given size have also been seen in active galaxies, for example, in the irregular galaxies NGC 4526 and II Zw 40 (Utomo et al. 2015; Kepley et al. 2016), and in the spiral galaxies M51, NGC 253, NGC 5253 (Colombo et al. 2014; Leroy et al. 2015; Miura et al. 2018), all of them hosting starbursts.

In Figs. 11b and c, corresponding to the luminosity-size and luminosity-linewidth relations, the offset of the SMC clouds from the Milky Way luminosity-scaling relations is also observed in the sample of low-metallicity galaxies with radii larger than 1 pc (discussed in Sect. 4.2.2). These clouds tend to be less luminous for a given size and more luminous for a given linewidth. In contrast, for a fixed luminosity, the CO clouds of these irregular galaxies are larger in size and less turbulent than those of the Milky Way. Interestingly, for 30 Doradus, the offsets in these luminosity scaling relations are in opposite directions, and have clouds that are smaller but more turbulent than those predicted by the relation of Solomon et al. (1987). We note, however, that the apparent offsets in both luminosity-scaling relations approximately cancel out in the virial mass calculation independently of the spatial resolution of the observations, so the correlation of CO-determined virial mass with CO luminosity (panel d of Fig. 11) follows a trend very similar to that of the Milky Way.

Despite the large scatter observed in the four scaling relations of Fig. 11, the low-metallicity irregular galaxies appear to follow a similar increasing trend over a wide dynamic range of $R \sim 1$ to 120 pc, $\sigma_v \sim 0.5$ to 10 km s^{-1}, $L_{CO} \sim 10^1$ to 10^6 K km s^{-1} pc^2, and $M_{vir} \sim 10^2$ to 10^7 $M_\odot$. However, these metal-poor galaxies seem to have systematic departures with respect to the standard Milky Way scaling relations, which could be due to intrinsic characteristics of the galaxies.

6. Summary and conclusions

We presented a CO(2−1) emission survey in the SMC with the APEX single-dish telescope at ∼9 pc resolution. We identified a total of 177 clouds using the CPROPS algorithm (Rosolowsky & Leroy 2006), 124 of which are bright ($S/N > 5$) and well-resolved clouds with radii between 2 to 13 pc, velocity dispersions of 0.4–3.2 km s^{-1}, CO luminosities between ∼66–7 × 10^3 K km s^{-1} pc^2, and virial masses of ∼7 × 10^2 – 10^5 $M_\odot$. The total luminosity of the identified 177 CO clouds is 1.3 × 10^5 K km s^{-1} pc^2. We note that we estimated ∼30% of the total CO luminosity in the investigated regions is not assigned to CO clouds.

We found that, on average, the SMC clouds are less turbulent, by a factor of approximately 2 than the inner Milky Way clouds (Solomon et al. 1987) of similar size (see also Bolatto et al. 2008). This shift was observed for all of our SMC clouds, independently of the region in which they are located. This feature is also shared with other low-metallicity galaxies at scales larger than 1 pc. The most probable explanation is that the CO components are in the innermost regions of the entire molecular cloud (Bolatto et al. 2008). However, we also highlight that the poor metal abundance can be an important factor that contributes to the turbulent deficiency (Braine et al. 2018).

We also found an agreement between the luminosity scaling relations of the SMC clouds with those of low-metallicity galaxies. Generally, clouds in low-metallicity galaxies have larger sizes and smaller linewidths at a fixed CO luminosity than their inner Milky Way counterparts. On sub-parsec scales, the relations show increased scatter and higher departures, although all clouds tend to follow a fairly tight $L_{CO} - M_{vir}$ relation.

We obtained the cumulative mass distribution for the SMC clouds using both their luminous and virial mass. Fitting the mass distribution (50 clouds above the completeness limit), we found power-law exponent $\beta \lesssim -2$ in both mass distributions with a weak truncated end and a maximum mass of $M_0 = 3.8 \times 10^4$ $M_\odot$ for the luminous mass distribution, and essentially negligible truncation for the virial mass distribution with a $M_0 = 14.2 \times 10^4$ $M_\odot$. The fitted maximum masses for the luminous and virial mass distributions of the SMC are about one order of magnitude lower than those of the LMC. Our results indicate that the molecular mass associated with CO clouds in the SMC is dominated by low-mass clouds across the galaxy.

We studied the stability of the SMC clouds by comparing their virial masses (from our CO emission) with their dust mass from 1.1 mm observations at 12 pc resolution (Takekoshi et al. 2017). We found that the SMC clouds are approximately in gravitational virial equilibrium, with the smaller clouds appearing less bounded.

We estimated a virial mass-based CO-to-H_2 conversion factor for the well-defined SMC clouds at 9 pc resolution. We obtained a median value of $\alpha^{vir}_{CO(1\text{-}0)} = 10.5 \pm 5$ $M_\odot$ (K km s^{-1} pc^2)$^{-1}$. This conversion factor is 2.5 times the canonical Galactic value (see Bolatto et al. 2013), but we also showed it is not inconsistent with the expectation for similarly luminous clouds in the Milky Way. We estimated the dust-based CO-to-H_2 conversion factors (as upper limits) for 19

dust clouds (Takekoshi et al. 2017) at 12 pc resolution within our observed area, finding a median value of $\alpha_{\rm CO(1-0)}^{\rm dust} = 28 \pm 15\ M_\odot\,(\mathrm{K\,km\,s^{-1}\,pc^2})^{-1}$, which is 6.5 times the Galactic value.

Finally, we found that the SMC clouds are mostly spatially associated with YSOs (43%) and barely associated with HII regions (24%). The YSOs associated with the CO clouds are luminous ($L_* \gtrsim 10^3\ L_\odot$) and massive ($M_* \gtrsim 8\,M_\odot$), and most of them are in an early evolutionary stage (stage I) where accretion is considerable. Notably, there is a poor association of clouds with more evolved YSOs (stages II/III). However, the HII regions would preferentially be interacting with large, luminous, and massive clouds. Our analysis also shows that about half of the clouds are associated with ongoing star formation (either YSOs or HII regions) but also that close to half of the clouds are not.

Acknowledgements. H.P.S. acknowledges partial financial support from a fellowship from Consejo Nacional de Investigación Científicas y Técnicas (CONCET-Argentina), and from Secretaría de Ciencias y Técnicas (SeCyT), Córdoba, Argentina, and partial support from ANID(CHILE) through FONDECYT grant No1190684. H.P.S. also thanks to E. Rosolowsky for sharing the IDL algorithm for the mass spectrum. M.R. wishes to acknowledge support from ANID(CHILE) through FONDECYT grant No1190684, and partial support from ANID project Basal AFB-170002, and Basal FB210003. A.D.B. acknowledges partial support from NSF-AST2108140. This publication is based on data acquired with the Atacama Pathfinder Experiment (APEX) under program ID (C093.F-9711A-2014) and (C.095F-9705A-2015) in Chile observing time. APEX is a collaboration between the Max-Planck-Institut fur Radioastronomie, the European Southern Observatory, and the Onsala Space Observatory.

References

Bolatto, A. D., Leroy, A., Israel, F. P., & Jackson, J. M. 2003, ApJ, 595, 167
Bolatto, A. D., Leroy, A. K., Rosolowsky, E., Walter, F., & Blitz, L. 2008, ApJ, 686, 948
Bolatto, A. D., Wolfire, M., & Leroy, A. K. 2013, ARA&A, 51, 207
Bot, C., Boulanger, F., Rubio, M., & Rantakyro, F. 2007, A&A, 471, 103
Bot, C., Rubio, M., Boulanger, F., et al. 2010, A&A, 524, A52
Braine, J., Rosolowsky, E., Gratier, P., Corbelli, E., & Schuster, K. F. 2018, A&A, 612, A51
Camacho, V., Vázquez-Semadeni, E., Ballesteros-Paredes, J., et al. 2016, ApJ, 833, 113
Carlson, L. R., Sewiło, M., Meixner, M., et al. 2011, ApJ, 730, 78
Colombo, D., Hughes, A., Schinnerer, E., et al. 2014, ApJ, 784, 3
Corbelli, E., Braine, J., Bandiera, R., et al. 2017, A&A, 601, A146
Dame, T. M. 2011, ArXiv e-prints [arXiv:1101.1499]
Di Teodoro, E. M., McClure-Griffiths, N. M., Jameson, K. E., et al. 2019, MNRAS, 483, 392
Fukui, Y., Ohno, T., Tsuge, K., Sano, H., & Tachihara, K. 2020, PASJ, submitted [arXiv:2005.13750]
Gordon, K. D., Meixner, M., Meade, M. R., et al. 2011, AJ, 142, 102
Gordon, K. D., Roman-Duval, J., Bot, C., et al. 2014, ApJ, 797, 85
Gouliermis, D. A., Schmeja, S., Dolphin, A. E., et al. 2012, Apj, 748, 64
Gratier, P., Braine, J., Rodriguez-Fernandez, N. J., et al. 2012, A&A, 542, A108
Güsten, R., Nyman, L. Å., Schilke, P., et al. 2006, A&A, 454, L13
Herrera, C. N., Rubio, M., Bolatto, A. D., et al. 2013, A&A, 554, A91
Heyer, M. H., Carpenter, J. M., & Snell, R. L. 2001, ApJ, 551, 852
Hilditch, R. W., Howarth, I. D., & Harries, T. J. 2005, MNRAS, 357, 304
Hocuk, S., & Spaans, M. 2010, A&A, 510, A110
Hony, S., Gouliermis, D. A., Galliano, F., et al. 2015, MNRAS, 448, 1847
Indebetouw, R., Brogan, C., Chen, C. H. R., et al. 2013, ApJ, 774, 73
Israel, F. P., Johansson, L. E. B., Lequeux, J., et al. 1993, A&A, 276, 25
Israel, F. P., Johansson, L. E. B., Rubio, M., et al. 2003, A&A, 406, 817
Jameson, K. E., Bolatto, A. D., Leroy, A. K., et al. 2016, ApJ, 825, 12
Jameson, K. E., Bolatto, A. D., Wolfire, M., et al. 2018, ApJ, 853, 111
Kaczmarek, J. F., Purcell, C. R., Gaensler, B. M., McClure-Griffiths, N. M., & Stevens, J. 2017, MNRAS, 467, 1776
Kalari, V. M., Rubio, M., Elmegreen, B. G., et al. 2018, ApJ, 852, 71
Kalari, V. M., Rubio, M., Saldaño, H. P., & Bolatto, A. D. 2020, MNRAS, 499, 2534
Kepley, A. A., Leroy, A. K., Johnson, K. E., Sandstrom, K., & Chen, C. H. R. 2016, ApJ, 828, 50
Leroy, A. K., Bolatto, A., Gordon, K., et al. 2011, ApJ, 737, 12
Leroy, A. K., Bolatto, A. D., Ostriker, E. C., et al. 2015, ApJ, 801, 25
Leroy, A. K., Hughes, A., Schruba, A., et al. 2016, ApJ, 831, 16
Lobo Gomes, A., Magalhães, A. M., Pereyra, A., & Rodrigues, C. V. 2015, ApJ, 806, 94
Miura, R. E., Espada, D., Hirota, A., et al. 2018, ApJ, 864, 120
Mizuno, N., Rubio, M., Mizuno, A., et al. 2001, PASJ, 53, L45
Muller, E., Ott, J., Hughes, A., et al. 2010, ApJ, 712, 1248
Muraoka, K., Homma, A., Onishi, T., et al. 2017, ApJ, 844, 98
Oka, T., Hasegawa, T., Sato, F., et al. 2001, ApJ, 562, 348
Ossenkopf, V., & Henning, T. 1994, A&A, 291, 943
Paradis, D., Bernard, J. P., Mény, C., & Gromov, V. 2011, A&A, 534, A118
Pellegrini, E. W., Oey, M. S., Winkler, P. F., et al. 2012, ApJ, 755, 40
Pineda, J. L., Langer, W. D., Goldsmith, P. F., et al. 2017, ApJ, 839, 107
Requena-Torres, M. A., Israel, F. P., Okada, Y., et al. 2016, A&A, 589, A28
Roman-Duval, J., Gordon, K. D., Meixner, M., et al. 2014, ApJ, 797, 86
Roman-Duval, J., Bot, C., Chastenet, J., & Gordon, K. 2017, ApJ, 841, 72
Rosolowsky, E. 2005, PASP, 117, 1403
Rosolowsky, E., & Leroy, A. 2006, PASP, 118, 590
Rubio, M., Garay, G., Montani, J., & Thaddeus, P. 1991, ApJ, 368, 173
Rubio, M., Lequeux, J., & Boulanger, F. 1993a, A&A, 271, 9
Rubio, M., Lequeux, J., Boulanger, F., et al. 1993b, A&A, 271, 1
Rubio, M., Lequeux, J., Boulanger, F., et al. 1996, A&As, 118, 263
Rubio, M., Contursi, A., Lequeux, J., et al. 2000, A&A, 359, 1139
Rubio, M., Elmegreen, B. G., Hunter, D. A., et al. 2015, Nature, 525, 218
Rubio, M., Barbá, R. H., & Kalari, V. M. 2018, A&A, 615, A121
Russell, S. C., & Dopita, M. A. 1992, ApJ, 384, 508
Saldaño, H. P., Rubio, M., Jameson, K., & Bolatto, A. D. 2018, Bol. Asoc. Argentina Astron. Plata Argentina, 60, 192
Schruba, A., Leroy, A. K., Kruijssen, J. M. D., et al. 2017, ApJ, 835, 278
Sewiło, M., Carlson, L. R., Seale, J. P., et al. 2013, ApJ, 778, 15
Simon, J. D., Bolatto, A. D., Whitney, B. A., et al. 2007, ApJ, 669, 327
Solomon, P. M., Rivolo, A. R., Barrett, J., & Yahil, A. 1987, ApJ, 319, 730
Takekoshi, T., Minamidani, T., Komugi, S., et al. 2017, ApJ, 835, 55
Tokuda, K., Kondo, H., Ohno, T., et al. 2021, ApJ, 922, 171
Utomo, D., Blitz, L., Davis, T., et al. 2015, ApJ, 803, 16
Valdivia-Mena, M. T., Rubio, M., Bolatto, A. D., Saldaño, H. P., & Verdugo, C. 2020, A&A, 641, A97
Vangioni-Flam, E., Lequeux, J., Maucherat-Joubert, M., & Rocca-Volmerange, B. 1980, A&A, 90, 73
Vassilev, V., Meledin, D., Lapkin, I., et al. 2008, A&A, 490, 1157
Ward, J. L., Oliveira, J. M., van Loon, J. T., & Sewiło, M. 2017, MNRAS, 464, 1512
Winkler, P. F., Smith, R. C., Points, S. D., & MCELS Team. 2015, ASP Conf. Ser., 491, 343
Wong, T., Hughes, A., Ott, J., et al. 2011, ApJS, 197, 16
Wong, T., Hughes, A., Tokuda, K., et al. 2019, ApJ, 885, 50

Appendix A: CPROPS application

We used the CPROPS algorithm to find the CO clouds (Rosolowsky & Leroy 2006) within our data cubes. For the decomposition method, we chose the modified CLUMPFIND algorithm (hereafter referred to as ECLUMP). As explained by the authors, the algorithm can be divided into two main parts: the signal identification and cloud decomposition. In the signal identification, the algorithm considers adjacent channels with intensities above a threshold (THRESH $\times \sigma_{\rm rms}$) to make a mask. Then, the mask is expanded to include all emissions above an edge threshold (EDGE $\times \sigma_{\rm rms}$) in the position-position-velocity cube (by default, the free parameters THRESH and EDGE have values of four and two, respectively). In all our observed regions, we mostly used THRESH = 3 and EDGE = 1.7 for signal identification.For a few clouds in the NE-Bar, SW-Bar, and DarkPK regions, an EDGE of 2.0–2.5 was used. For weak signals in three isolated regions in the NE-Bar, the EDGE parameter was reduced to a value of 1.2–1.5. In this step, we obtained masks with the most significant emissions, which are defined as "islands" and may be composed of local maxima (substructures) that have to be decomposed. Finally, we flagged the substructures as true or false clouds. We considered the substructures true clouds if they had areas (MINAREA) larger than the beam size and velocity widths (MINVCHAN) greater than or equal to four channels (1.0 km s^{-1}) in the decomposition.

In some cases, we rescaled the data to reduce the contrast between very close substructures in order to merge them into one cloud when the decomposition was not reliable (i.e., two very close unresolved clouds into one resolved cloud). The parameter that handles the contrast is called BCLIP. We only used BCLIP = 2.4 for a few clouds in the SW-Bar. In DarkPK, the decomposition was forced to merge a couple of clouds, making BCLIP = 0.2.

The CPROPS algorithm corrects for a substantial sensitivity bias by extrapolating each measured property of a cloud to find the value expected by perfect sensitivity (rms brightness temperature $T_{\rm rms}$ = 0 K). The extrapolation causes an enlargement effect on the parameter. Then, the measured properties are corrected for the resolution bias by using the beam size ($\sigma_{\rm beam}$) and the width of the velocity channel through Equations 9 and 10 from Rosolowsky & Leroy (2006). It is important to note that both the cloud size and velocity dispersion are defined as rms sizes of the intensity distribution along the two spatial and spectral dimensions, respectively, and these values increase when the data dispersion within the decomposed substructure are much higher.

Appendix B: CO(2–1) and star-forming regions in the SMC

Figures B.1 to B.7 show the good spatial correlation of the CO emission with the star-forming regions traced by Hα, *Spitzer* 8 μm, Herschel 160 μm, and 1.1 mm in the surveyed regions of the SMC. In general, the CO emission coincides spatially with peak emission at 8 μm, 160 μm, and 1.1 mm, indicating important star formation in these molecular clouds. The DarkPK region is an exception since weak or no emission was detected at these wavelengths (Fig. B.5), suggesting that the DarkPK is a quiescent region with a reduced high-mass star formation (see Jameson et al. 2018). Similarly, some small CO clouds in the SW-Bar and NE-Bar have weak or no emission at any of these star formation tracers, indicating quiescent molecular clouds.

We show the YSO candidates selected from Simon et al. (2007), Carlson et al. (2011), and Sewiło et al. (2013) on the 8 μm maps of the observed regions (Figs. B.1–B.7). These YSOs have been classified according to their sequential evolutive stages (I, II, and III), which are determined by the modeling of their SEDs and the gas mass accretion criteria. We observed that the CO distribution agrees well with the youngest YSOs (Stage I), while a poorer association is found for more evolved YSOs (Stages II and III). Comparing the position of the YSOs to the CO cloud center (see Sect. 4.3), we found that 94 YSOs with defined evolutive stages are associated with CO clouds in our observed maps. Of these, 60% are Stage I YSOs, 16% are Stages II and III, and 24% are undefined YSOs. Although these proportions are dependent on the completeness of the existing YSO catalogs as well as the sensitivity of CO observations, we expect the Stage I YSOs to continue to show high probabilities of being associated with molecular clouds.

Appendix B.1. Particular regions of the SMC

In this section, we describe the association of the star-formation signposts with the molecular clouds in N66, N83, N88, and DarkPk regions observed in the SMC. In each region, we consider the association with 8 μm, Hα and 1.1 mm emission with the CO gas distribution.

The N66 region is the brightest HII region in the SMC and is characterized by extended gas emission ionized by the stellar cluster NGC 346. The CO gas distribution in the vicinity of NGC 346 follows an arc-like structure extending from the NW to the SE and is associated with filaments at 8 μm and peak emission at Hα and 1.1 mm (see Fig. B.3). In the same line of sight to NGC 346, there are two molecular clouds (IDs 105 and 106 in Table 2), despite the presence of a strong radiation field. Both clouds, have a high S/N > 5, show a large velocity separation of about 15 km s^{-1} of difference in their peak velocities, and have the widest linewidths ($\sigma_v \approx 2$ km s^{-1}) of the NE clouds (see Fig. 4). These large linewidths in both clouds may indicate a tight interaction with NGC 346, whereas the large separation in velocity may confirm that the ISM in N66 seems to be lacerated by ionized gas, as suggested by Hony et al. (2015). Embedded young massive stars have been spectroscopically identified in the near IR toward CO clouds in N66 (Rubio et al. 2018).

Perpendicular to the arc-like bar in the NE direction of N66, there is the strongest but densest and also cold CO gas (plume-like structure) in N66 (see Rubio et al. 2000; Requena-Torres et al. 2016), with strong emission at 8 μm (not associated with Stage I YSOs) but weak emission at Hα and 1.1 mm. Finally, a weak CO cloud was detected to the southwest of N66, likely a quiescent cloud since no association with YSOs was found and only weak emissions at 8 μm and 1.1 mm were detected.

The N83 region is an isolated, relatively active star formation region with several cataloged molecular clouds. Some of clouds lie between two extended Hα emissions, and one of them hosts the NGC 456 cluster, in the southernmost part of N83 (Fig. B.4). There are four other more compact HII regions in the area closer to the brightest CO clouds. Two of these clouds (IDs 158 and 160 in Table 2) have the highest CO luminosity of the WG clouds, with $L_{\rm CO} > 2 \times 10^3$ K km s^{-1} pc^2. These clouds could be associated with an expanding shell of NGC 456, although there is no clear evidence of whether these bright clouds are being swept up by the expanding shell of the HII region NGC 456, or they are only ambient clouds interacting with the ionized gas (Bolatto et al. 2003). The third most luminous cloud (ID 165),

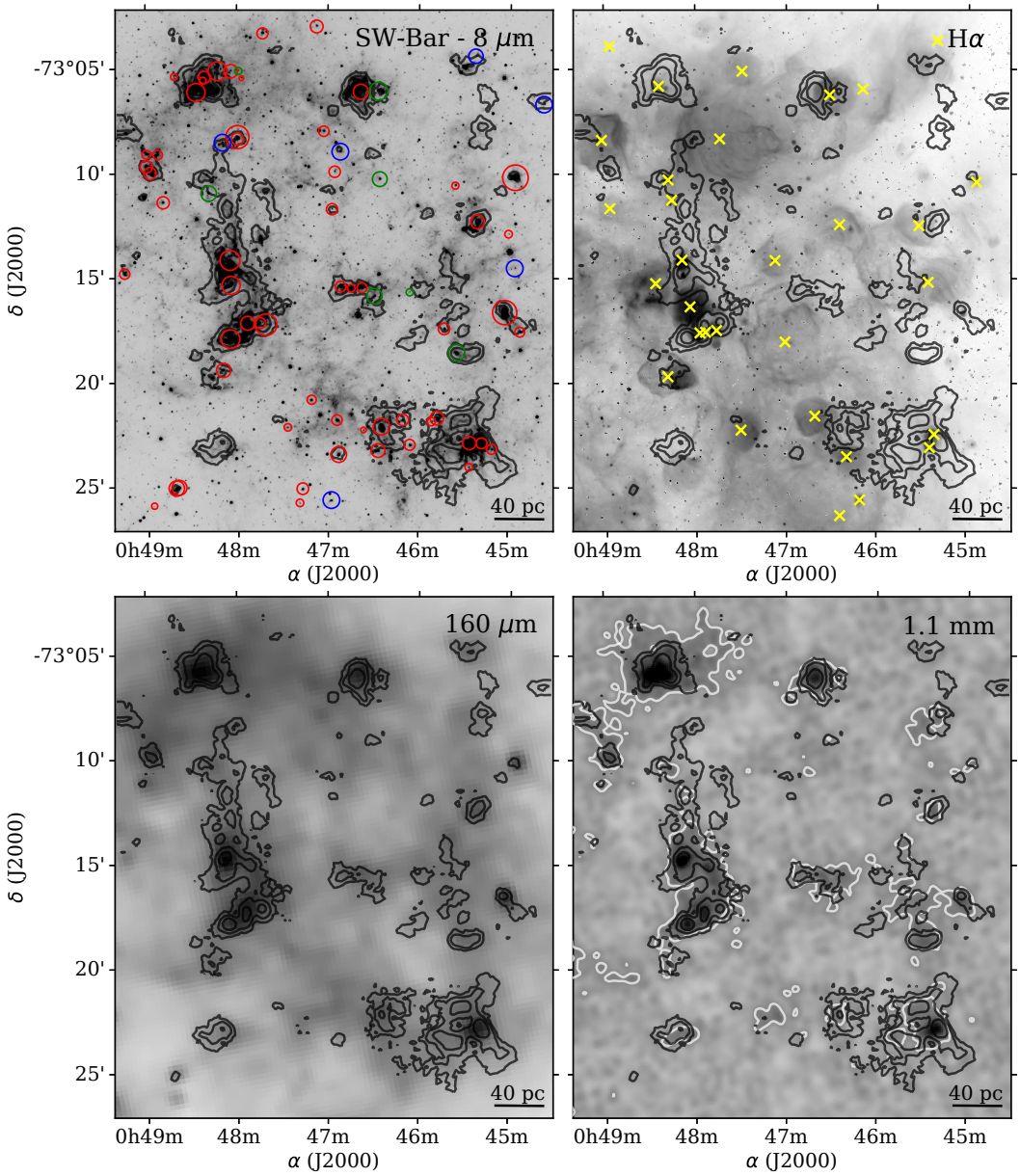

Fig. B.1. CO(2−1) emission at 9 pc resolution (black contours) in the SW-Bar superimposed to the *Spitzer* 8 μm map (upper-left), MCELS Hα map (upper-right), Herschel 160 μm map (bottom-left), and AzSTEC 1.1 mm map (bottom-right). The CO contours correspond to 1.5, 4.5, and 10.0 K km s^{-1}. An evolutionary classification of YSOs from Sewiło et al. (2013) and Simon et al. (2007) are indicated by red (Stage I), green (Stage II), and blue (Stage III) circles in the upper-left panel. The sizes of these circles are proportional to the stellar luminosity. In the upper-right panel, the "×" symbols show the location of the HII regions identified by Pellegrini et al. (2012). In the bottom-right panel, the white contours indicate the 1.1 mm emission at 5σ.

with $L_{CO} \simeq 1.2 \times 10^3$ K km s^{-1} pc^2, is associated with the HII region located toward the northeast direction of NGC 456.

In particular, these three very luminous clouds show smaller radii and linewidths than the SMC clouds of similar luminosity and, in consequence, lower M_{vir} than their SW and NE counterparts (see Fig. 6). Such features may be attributed to their interaction with the expanding shell of the HII regions in N83.

The DarkPK region is one of the more quiescent regions of the SMC. Figure B.5 shows the CO distribution slightly correlated with the 8 μm emission and not correlated with the Hα emission, and only one YSO (Stage I) is associated with a CO clump. At longer wavelengths, the CO clouds show a better association with warm dust at 160 μm than than cool dust emission not detected at 1.1 mm (Takekoshi et al. 2017). These associations correlate well with the finding from Jameson et al. (2018) in the DarkPK. These authors observed low levels of CO(2−1) and atomic ([CII], [OI]) emissions. They derived an averaged $N_{H2} \approx 0.5 \times 10^{21}$ cm^{-3} that is about two to six times lower than those of CO-bright regions in the SW-Bar. They also estimated a very low A_V with a mean value of ∼0.8 mag, which is consistent with the very low CO and H_2 abundance.

The HII complex NGC602/N90 is characterized by two ridges of dust filaments toward the southeast and northwest (see Fig. B.6) and an ionized cavity near the bright young stellar cluster NGC 602. The region harbors tens of massive YSOs (see Carlson et al. 2011), most of them of Stage I over the ridges. Our three CO clouds (IDs 175, 176, and 177 in Table 2) located in the outskirts of the main cluster coincide with the location of Stage I YSOs and smaller pre-main sequence (PMS) subclusters (Gouliermis et al. 2012). The central cluster, NGC 602,

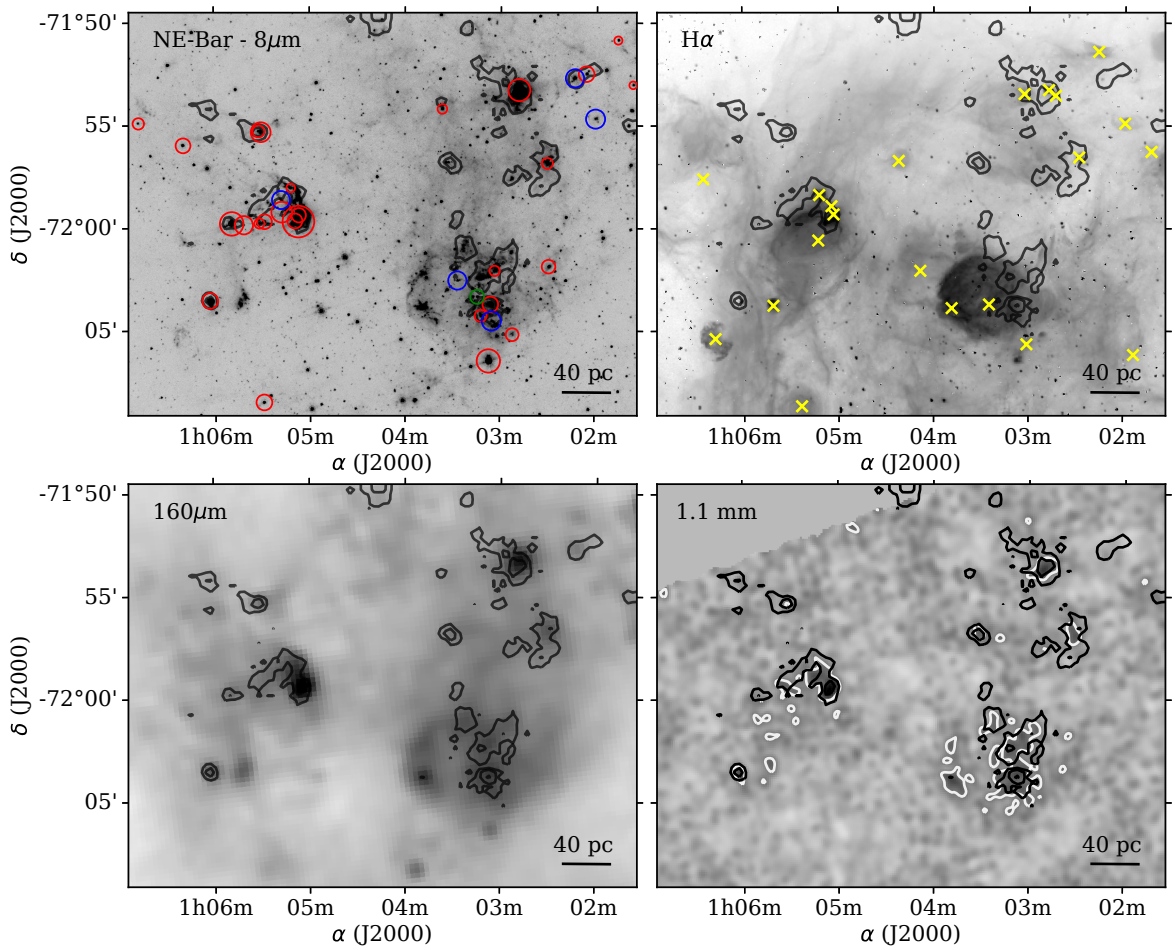

Fig. B.2. Similar to Fig. B.1 but for NE-Bar. The CO(2−1) emission, black contours, have values of 1.0, 2.0, and 4.5 K km s^{-1}.

seems to have blown all the molecular gas beyond an average distance of ∼12 pc (see Carlson et al. 2011), which is where the YSOs and CO gas are located (see also Fukui et al. 2020). The association of the three CO clouds with warm dust emission detected at 160 μm (denser in the SE ridge) may explain the shielding of these three clouds. The high radiation field produced in the vicinity of NGC 602 may be heating the environment at considerable temperatures, so the cold dust emission at 1.1 mm would not be detected in the region. In fact, cold dust emission is extremely rare in the Wing and Magellanic Bridge as was shown by Takekoshi et al. (2017) and Valdivia-Mena et al. (2020).

In the N88 region, only one molecular cloud was found. This cloud is in the line of sight of a strong source at 8 μm and Hα (Fig. B.7). Most of the short wavelength emission comes from the ultra-compact (UC) HII region N88-A excited by zero-age main-sequence massive stars of spectral type O6 (Ward et al. 2017). Spectroscopic studies in Brγ 2.1661 μm and H_2 2.1218 μm emission lines (Ward et al. 2017) show an arc-like H_2 structure that is associated with an expanding ionized Brγ gas whose line emissions peak at heliocentric centroid velocities of 153 − 156 km s^{-1} (V_{lsr} = 144 − 147 km s^{-1}). The CO cloud in this region (ID 174 in Table 2) has a peak emission at V_{lsr} = 147.6 km s^{-1}, quite similar to that of the main Brγ component (#35A) at V_{lsr} = 146.8 km s^{-1} (Ward et al. 2017). Therefore, it is most likely that the UC HII region and the CO cloud are associated. As expected, the molecular cloud is associated with compact emission at 160 μm and 1.1 mm, consistent with CO being protected from the high radiation field of the UC ionized region. In fact, the high H_2 density in this region (approximately three to ten times higher than that in N66, see Requena-Torres et al. 2016) estimated from [CII] emission would prevent the fast photodissociation of the CO cloud in the most extreme environments of the SMC.

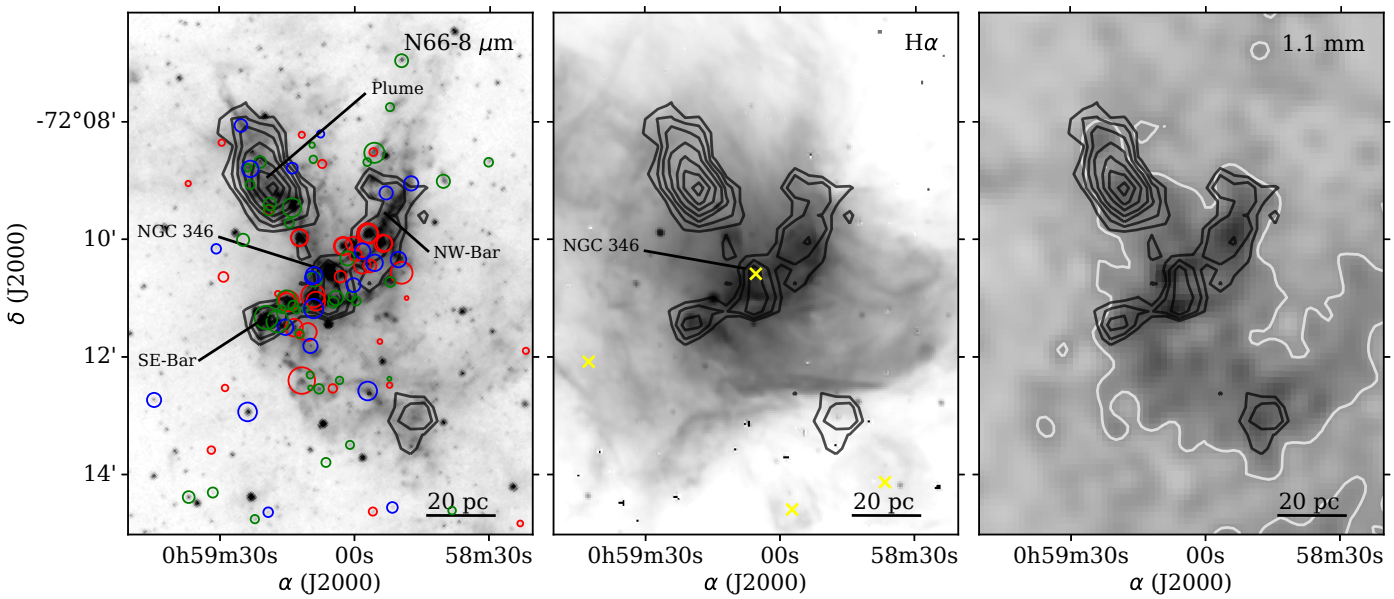

Fig. B.3. CO(2−1) emission toward N66 (black contours at levels 1.6, 2.6, 4.0, 5.7, 8.6, 11.4, and 14.3 K km s^{-1}) superimposed to the *Spitzer* 8 μm (left), MCELS Hα (middle), and AzTEC 1.1 mm (right) maps. An evolutionary classification of YSOs from Sewiło et al. (2013) and Simon et al. (2007) is indicated by red (Stage I), green (Stage II), and blue (Stage III) circles. The sizes of these circles are proportional to the stellar luminosity. The main cluster of N66 (NGC 346), the plume, and the bar structures are indicated. Yellow "×" symbols in the middle panel indicate the HII regions from Pellegrini et al. (2012). In the right panel, the 1.1 mm emission at 5σ is highlighted.

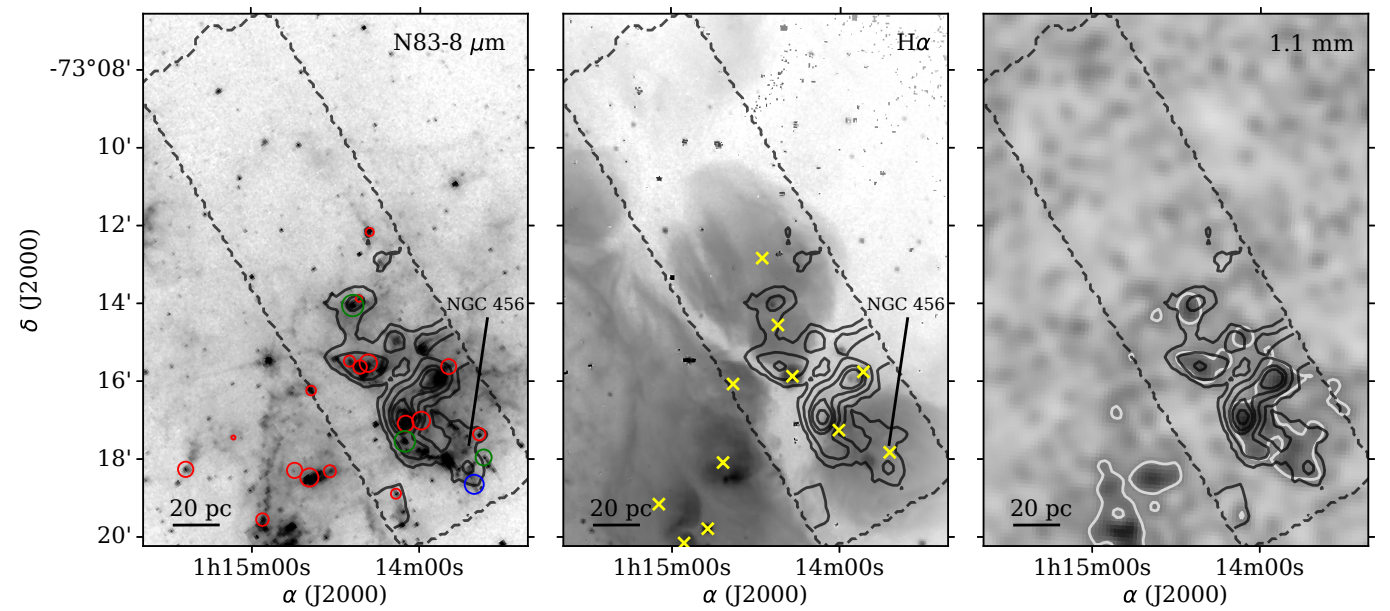

Fig. B.4. Similar to Fig. B.3 but for N83. The CO(2−1) emissions, black contours, have values of 1, 3, 7, 10, and 15 K km s^{-1}.

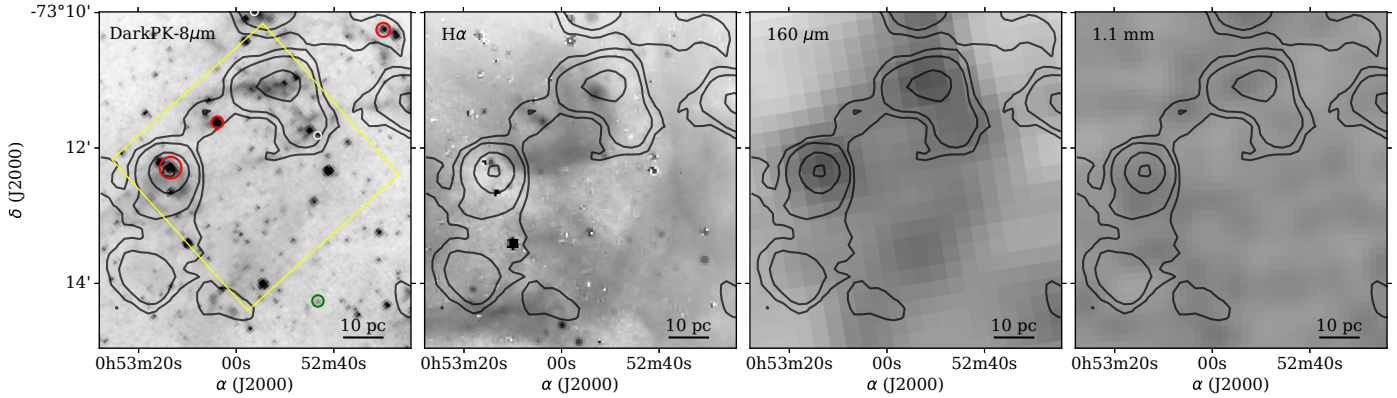

Fig. B.5. CO(2−1) emission toward DarkPK (black contours at levels 0.5, 1.0, 3.0, and 6.0 K km s^{-1}) superimposed to the *Spitzer* 8 μm, MCELS Hα, Herschel 160 μm, and AzTEC 1.1 mm maps. The evolutionary classification of YSOs from Sewiło et al. (2013) is indicated by red (Stage I) and green (Stage II) circles. The sizes of these circles are proportional to the stellar luminosity. The yellow box in the 8 μm map indicates the regions where CO emission was detected with ALMA by Jameson et al. (2018).

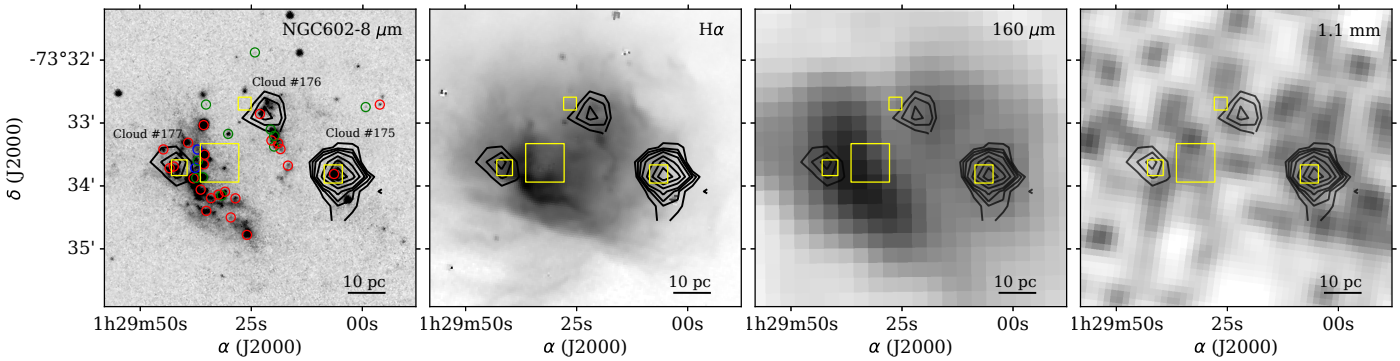

Fig. B.6. CO(2−1) emission toward NGC 602 (black contours at levels 0.4, 0.5, 0.6, 0.9, 1.3, 1.7, and 2.1 K km s^{-1}) superimposed to the *Spitzer* 8 μm, MCELS Hα, Herschel 160 μm, and AzTEC 1.1 mm maps. The IDs of the three clouds correspond to Table 2. The evolutionary classification of YSOs from Carlson et al. (2011) are indicated by red (Stage I), green (Stages I-II and II), and blue (Stages II-III and III) circles. The largest yellow square represents the main stellar cluster, and the smaller squares indicate PMS subclusters (see Gouliermis et al. 2012) associated with the CO emission.

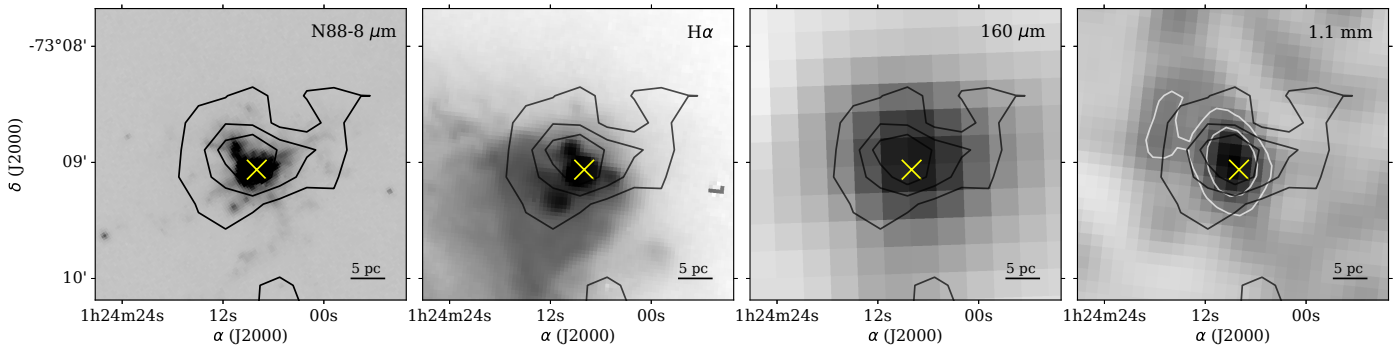

Fig. B.7. CO(2−1) emission toward N88 (black contours at levels 1.4, 2.8, and 4.3 K km s^{-1}) superimposed to the *Spitzer* 8 μm band, MCELS Hα, Herschel 160 μm, and AzTEC 1.1 mm maps. White contours highlight the continuum 1.1 mm emission. The "×" symbols indicate the position of the UC HII region N88-A.